PHYSICAL REVIEW D **74,** 104005 (2006)

Transition from inspiral to plunge in precessing binaries of spinning black holes

Alessandra Buonanno*
AstroParticule et Cosmologie (APC), 11 place Marcelin Berthelot, 75005 Paris, France

Yanbei Chen
Max-Planck-Institut für Gravitationsphysik (Albert-Einstein-Institut), Am Mühlenberg 1, D-14476 Golm bei Potsdam, Germany

Thibault Damour
Institut des Hautes Etudes Scientifiques, 91440 Bures-sur-Yvette, France
(Received 8 November 2005; published 2 November 2006)

We investigate the nonadiabatic dynamics of spinning black-hole binaries by using an analytical Hamiltonian completed with a radiation-reaction force, containing spin couplings, which matches the known rates of energy and angular-momentum losses on quasicircular orbits. We consider both a straightforward post-Newtonian-expanded Hamiltonian (including spin-dependent terms), and a version of the resummed post-Newtonian Hamiltonian defined by the effective one-body approach. We focus on the influence spin terms have on the dynamics and waveforms. We evaluate the energy and angular momentum released during the final stage of inspiral and plunge. For an equal-mass binary the energy released between 40 Hz and the frequency beyond which our analytical treatment becomes unreliable is found to be, when using the effective one-body dynamics, $0.6\%M$ for antialigned maximally spinning black holes, $5\%M$ for aligned maximally spinning black holes, and $1.8\%M$ for nonspinning configurations. In confirmation of previous results, we find that, for all binaries considered, the dimensionless rotation parameter J/E^2 is always smaller than unity at the end of the inspiral, so that a Kerr black hole can form right after the inspiral phase. By matching a quasinormal mode ring down to the last reliable stages of the plunge, we construct complete waveforms approximately describing the gravitational-wave signal emitted by the entire process of coalescence of precessing binaries of spinning black holes.

DOI: 10.1103/PhysRevD.74.104005 PACS numbers: 04.30.Db, 04.25.Nx, 04.70.Bw, 04.80.Nn

I. INTRODUCTION

An international network of kilometer-scale laser-interferometric gravitational-wave detectors, consisting of the Laser-Interferometer Gravitational-wave Observatory (LIGO) [1], VIRGO [2], GEO 600 [3], and TAMA 300 [4], has by now begun the science operations. TAMA 300 reached its full design sensitivity in 2001, VIRGO is in its commissioning phase and plans to start the first scientific runs by the end of the year, while LIGO has already completed three science runs (two of them in coincidence with GEO 600) with increasing sensitivity and duty cycle. LIGO started the one-year run at design sensitivity in November 2005.

Binary black holes are among the most promising sources for these detectors. Among black hole binaries, it was emphasized in [5] that there is a bias towards first detecting mostly aligned spinning binaries with high masses, whose last stable spherical orbits are drawn, by spin effects, to larger binding energies. Yet, due to their high masses, these energies are still emitted through gravitational waves in the sensitive band of the detectors. Studying in detail the waveforms emitted during the last stages of dynamical evolution of such heavy spinning black hole binaries, with explicit consideration of the crucial transition between adiabatic inspiral and plunge, is a demanding theoretical challenge. The aim of the present paper is to provide a first attack on this problem by using some of the best analytical tools currently available to describe the transition from adiabatic inspiral to plunge, notably the effective-one-body (EOB) approach [6,7].

So far, most theoretical and data-analysis studies on precessing binaries of spinning black holes assumed *adiabatic evolution*. Thus they were restricted to considering *only* the inspiral phase [8–18]. Actually, even for nonspinning binary configurations, most theoretical studies confined themselves to considering the adiabatic inspiral phase, though a lot of effort was spent to improve the accuracy of the phasing during the last stages of the inspiral; see e.g. [19,20].

For heavy black hole binaries, most of the signal-to-noise ratio in the ground detectors will come from the very last stages of the inspiral, and from the nonadiabatic transition between inspiral and plunge. It is therefore essential to be able to describe, with acceptable accuracy, this nonadiabatic evolution. In Refs. [6,7] a new way of describing the dynamics of binary systems was introduced: the EOB approach. The EOB approach uses both a specific resummation of the post-Newtonian Hamiltonian and a resummed version of radiation reaction (RR). This was shown to lead to a rather robust formalism, which we

*UMR 7164 (CNRS, Université Paris7, CEA, Observatoire de Paris). Also at Institut d'Astrophysique de Paris, 98bis Boulevard Arago, 75013 Paris, France.

 © 2006 The American Physical Society

expect (or hope) to provide a reliable description of nonadiabatic effects of the transition between inspiral and plunge, and of the beginning of the plunge. It was also used in [7] to model the full merger phase of nonspinning binaries, by matching the natural end of the EOB plunge with the ring-down phase. The EOB approach was used in Refs. [7,21] to derive nonadiabatic template waveforms emitted by *nonspinning* black hole binaries. It was shown in [22] that these new EOB templates led to enhanced signal-to-noise ratios in current detectors (mainly because of the inclusion of the plunge signal). The EOB Hamiltonian was extended to the case of spinning black holes in [5]. The analytical predictions made by the EOB method (including spin) were found to agree remarkably well [23] with the numerical results obtained by means of the helical Killing vector (HKV) approach [24] for circular orbits of corotating black holes. Several other studies showed that the EOB method provides phasing models which are more reliable and robust than other (adiabatic or nonadiabatic) models [25,26].

The main purpose of this paper is to extend the use of the EOB approach to the case of precessing binaries of spinning black holes, both by including spin-dependent terms in radiation-reaction effects, and by studying the waveforms generated beyond the adiabatic approximation, i.e. taking into account the transition between inspiral and plunge, and the plunge itself. Let us emphasize again that the EOB approach has the advantage of providing an *analytical* (but still approximate) description of the transition from inspiral to plunge. Recently, some attempts have been made to tackle, by means of 3D *numerical* simulations (combined with a perturbative approach), the gravitational radiation emitted by a very tight black hole binary both in nonspinning [27] and moderately spinning, but nonprecessing [28], configurations. These 3D simulations indicated the emission of a larger amount of energy in the form of gravitational radiation than what we shall find from our analytical, EOB approach.

Recent simulations [18] based on population synthesis codes predict that $\sim$50%–80% of neutron-star–black-hole (NS-BH) binaries in the galactic field may have tilt angles (i.e., the angle between the black hole (BH) spin and the orbital angular momentum) between 0° and 40° and 10%–20% of NS-BH binaries may have tilt angles between 40° and 50°. By studying the formation of close compact binaries and the misalignment angle that can occur after the second core-collapse event, Kalogera [29] predicted that the majority of BH-BH binaries in galactic binaries may have a tilt angle smaller than 30°. All these results assume that the misalignment is entirely due to the recoil velocity (''kick'') imparted to the NS (or the smaller BH in the binary) at birth by the core collapse. However, the spin properties of NS-BH and BH-BH binaries in a dense environment and centers of globular clusters could be very different than in the galactic field. Considering the low event rates, $\sim$1 per 2 years, of binary coalescences in the first generation of ground-based detectors, it is worthwhile to adopt a conservative point of view and investigate waveforms for generic spin configurations. Little is known about the magnitude of the spin of NSs and BHs. From the observed pulsars the dimensionless rotation parameter $a_{\rm NS}$ takes values in the range 0.005–0.02. Our analysis will focus on BH-BH binaries and we shall consider arbitrary spins: $0 < a_{\rm BH} < 1$.

For completeness, we investigate the two-body dynamics by adopting two approaches: the straightforward post-Newtonian (PN)-expanded Hamiltonian [30,31] and the PN-resummed Hamiltonian à la EOB [5,6,21] (henceforth referred to simply as the EOB Hamiltonian). For simplicity, instead of using the Kerr-deformed EOB Hamiltonian derived by Damour in Ref. [5], we shall use as the Hamiltonian in this paper the *sum* of the purely orbital (Schwarzschild-deformed) EOB Hamiltonian [6,21] and of the *separate* contributions due to spin-orbit and spin-spin effects. (Note that, among the spin-spin terms, there are the terms due to monopole-quadrupole interactions [5,32].)

The paper is organized as follows. Section II summarizes the main results of the conservative part of the two-body dynamics in the Hamiltonian formalism, and contains formulas for the PN-expanded and EOB Hamiltonians up to 3PN order. In Sec. III we augment the dynamics with radiation-reaction effects. We derive the radiation-reaction force which includes spin effects and matches known rates of energy and angular-momentum losses on quasicircular orbits. (Our result agrees with the recent results of Will [33] that appeared after we had completed our work.) In Sec. IV we define the two-body approximants and discuss the initial conditions used to evolve the precessing two-body dynamics; we compare the (lowest-order) waveforms obtained using PN-expanded and (PN-resummed) EOB dynamics by computing the overlaps between these two types of waveforms. Since only the EOB approach allows us to have robust predictions beyond the inspiral phase, we use them (and only them) to estimate the energy and angular momentum released during the last stages of evolution. Section VII contains our main conclusions.

We leave to future work a thorough application of our results to data analysis.

II. CONSERVATIVE HAMILTONIAN INCLUDING SPIN-ORBIT AND SPIN-SPIN EFFECTS

A. Orbital third-post-Newtonian expanded Hamiltonian

The purely *orbital* (nonspinning) third-post-Newtonian Hamiltonian $H^0 = H^0(\boldsymbol{X}, \boldsymbol{P})$ (in the center of mass frame, and after subtraction of the total rest-mass term) was derived in Ref. [31] (completed by Refs. [34,35]). In scaled variables, and written as a straigthforward PN expansion, it reads (see Ref. [21])

$$H^0(\boldsymbol{X},\boldsymbol{P})_{\rm EXP} = \mu\hat{H}^0(\boldsymbol{q},\boldsymbol{p}) = \mu[\hat{H}_{\rm Newt}(\boldsymbol{q},\boldsymbol{p}) + \hat{H}_{\rm 1PN}(\boldsymbol{q},\boldsymbol{p}) + \hat{H}_{\rm 2PN}(\boldsymbol{q},\boldsymbol{p}) + \hat{H}_{\rm 3PN}(\boldsymbol{q},\boldsymbol{p})], \tag{2.1}$$

where $\mu = m_1 m_2/M$, $M = m_1 + m_2$, and $(\boldsymbol{q},\boldsymbol{p})$ denote the canonical variables $\mathbf{p} \equiv \mathbf{P_1}/\mu = -\mathbf{P_2}/\mu$, and $\mathbf{q} \equiv \mathbf{X}/M = (\mathbf{X}_1 - \mathbf{X}_2)/M$, where $\mathbf{X_1}$ and $\mathbf{X_2}$ are the positions of the black hole centers of mass in quasi-Cartesian Arnowitt-Deser-Misner (ADM) coordinates. The Newtonian term and the PN contributions read (denoting $\eta \equiv \mu/M = m_1 m_2/M^2$)

$$\hat{H}_{\rm Newt}(\mathbf{q},\mathbf{p}) = \frac{\mathbf{p}^2}{2} - \frac{1}{q}, \tag{2.2}$$

$$\hat{H}_{\rm 1PN}(\mathbf{q},\mathbf{p}) = \frac{1}{8}(3\eta - 1)(\mathbf{p}^2)^2 - \frac{1}{2}[(3+\eta)\mathbf{p}^2 + \eta(\mathbf{n}\cdot\mathbf{p})^2]\frac{1}{q} + \frac{1}{2q^2}, \tag{2.3}$$

$$\hat{H}_{\rm 2PN}(\mathbf{q},\mathbf{p}) = \frac{1}{16}(1 - 5\eta + 5\eta^2)(\mathbf{p}^2)^3 + \frac{1}{8}[(5 - 20\eta - 3\eta^2)(\mathbf{p}^2)^2 - 2\eta^2(\mathbf{n}\cdot\mathbf{p})^2\mathbf{p}^2 - 3\eta^2(\mathbf{n}\cdot\mathbf{p})^4]\frac{1}{q} + \frac{1}{2}[(5+8\eta)\mathbf{p}^2 + 3\eta(\mathbf{n}\cdot\mathbf{p})^2]\frac{1}{q^2} - \frac{1}{4}(1+3\eta)\frac{1}{q^3}, \tag{2.4}$$

$$\begin{aligned}\hat{H}_{\rm 3PN}(\mathbf{q},\mathbf{p}) = {} & \frac{1}{128}(-5 + 35\eta - 70\eta^2 + 35\eta^3)(\mathbf{p}^2)^4 + \frac{1}{16}[(-7 + 42\eta - 53\eta^2 - 5\eta^3)(\mathbf{p}^2)^3 + (2 - 3\eta)\eta^2(\mathbf{n}\cdot\mathbf{p})^2(\mathbf{p}^2)^2 \\ & + 3(1-\eta)\eta^2(\mathbf{n}\cdot\mathbf{p})^4\mathbf{p}^2 - 5\eta^3(\mathbf{n}\cdot\mathbf{p})^6]\frac{1}{q} + \left[\frac{1}{16}(-27 + 136\eta + 109\eta^2)(\mathbf{p}^2)^2 \right. \\ & \left. + \frac{1}{16}(17 + 30\eta)\eta(\mathbf{n}\cdot\mathbf{p})^2\mathbf{p}^2 + \frac{1}{12}(5 + 43\eta)\eta(\mathbf{n}\cdot\mathbf{p})^4\right]\frac{1}{q^2} \\ & + \left\{\left[-\frac{25}{8} + \left(\frac{1}{64}\pi^2 - \frac{335}{48}\right)\eta - \frac{23}{8}\eta^2\right]\mathbf{p}^2 + \left(-\frac{85}{16} - \frac{3}{64}\pi^2 - \frac{7}{4}\eta\right)\eta(\mathbf{n}\cdot\mathbf{p})^2\right\}\frac{1}{q^3} \\ & + \left[\frac{1}{8} + \left(\frac{109}{12} - \frac{21}{32}\pi^2\right)\eta\right]\frac{1}{q^4},\end{aligned} \tag{2.5}$$

where the scalars q and p are the (coordinate) lengths of the two vectors $\boldsymbol{q}$ and $\boldsymbol{p}$, and the vector $\mathbf{n}$ is just $\mathbf{q}/q$.

B. Orbital third-post-Newtonian effective-one-body Hamiltonian

As was emphasized in previous work (see e.g. [36,37]), and as we shall confirm below, the nonresummed PN-expanded Hamiltonian (or the nonresummed PN-expanded equations of motion) does not lead to a reliable description of the evolution near the last stable circular orbit, nor *a fortiori* during the transition between inspiral and plunge. On the other hand, it was argued in [6,7,21] that the EOB approach defines a specific resummation of the PN-expanded Hamiltonian which leads to a much more robust description of the dynamical evolution near the last stable circular orbit, and of the transition between inspiral and plunge.

In the EOB approach for nonspinning binaries, the two-body dynamics is described in terms of a new set of canonical variables, $(\boldsymbol{X}', \boldsymbol{P}')$, which relate to $(\boldsymbol{X}, \boldsymbol{P})$ by a canonical transformation, given in Refs. [6,21] as explicit PN expansions. In $(\boldsymbol{X}', \boldsymbol{P}')$, the dynamics can be viewed as that of a single particle moving in a *deformed Schwarzchild spacetime* [6,21]. Namely, in these variables, the explicit expression of the purely orbital, EOB Hamiltonian is [6]

$$H^0_{\rm EOB}(\boldsymbol{X}', \boldsymbol{P}') = M\sqrt{1 + 2\eta\left(\frac{H_{\rm eff}(\boldsymbol{X}', \boldsymbol{P}') - \mu}{\mu}\right)} - M, \tag{2.6}$$

where $H_{\rm eff}$ is given by [6,21]

$$H_{\rm eff}(\boldsymbol{X}', \boldsymbol{P}') = \mu\hat{H}_{\rm eff}(\mathbf{q}', \mathbf{p}') = \mu\sqrt{A(q')\left[1 + \mathbf{p}'^2 + \left(\frac{A(q')}{D(q')} - 1\right)(\mathbf{n}'\cdot\mathbf{p}')^2 + \frac{1}{q'^2}(z_1(\mathbf{p}'^2)^2 + z_2\mathbf{p}'^2(\mathbf{n}'\cdot\mathbf{p}')^2 + z_3(\mathbf{n}'\cdot\mathbf{p}')^4)\right]}, \tag{2.7}$$

with $\mathbf{q}'$ and $\mathbf{p}'$ being the reduced canonical variables obtained by rescaling $\boldsymbol{X}'$ and $\boldsymbol{P}'$ by M and μ, respectively; $\mathbf{n}' = \boldsymbol{q}'/q'$ where we set $q' = |\mathbf{q}'|$. The coefficients z_1, z_2, and z_3 are arbitrary, subject to the constraint

$$8z_1 + 4z_2 + 3z_3 = 6(4 - 3\eta)\eta. \tag{2.8}$$

Setting (as in Ref. [25]) $z_1 = \eta\tilde{z}_1$, $z_2 = \eta\tilde{z}_2$, and $z_3 = \eta\tilde{z}_3$, the coefficients $A(q')$ and $D(q')$ in Eq. (2.7) read

$$A(q') = 1 - \frac{2}{q'} + \frac{2\eta}{q'^3} + \left[\left(\frac{94}{3} - \frac{41}{32}\pi^2\right) - \tilde{z}_1\right]\frac{\eta}{q'^4}, \tag{2.9}$$

$$D(q') = 1 - \frac{6\eta}{q'^2} + [7\tilde{z}_1 + \tilde{z}_2 + (3\eta - 26)]\frac{\eta}{q'^3}. \tag{2.10}$$

As done in Ref. [21], we restrict ourselves to the case $\tilde{z}_1 = \tilde{z}_2 = 0$ and improve the behavior[1] by replacing the "effective potential" $A(q')$ with the Padé approximants

$$A_{P_2}(q') = \frac{q'(-4 + 2q' + \eta)}{2q'^2 + 2\eta + q'\eta} \tag{2.11}$$

at 2PN order and

$$A_{P_3}(q') = \frac{q'^2[(a_4(\eta, 0) + 8\eta - 16) + q'(8 - 2\eta)]}{q'^3(8 - 2\eta) + q'^2(a_4(\eta, 0) + 4\eta) + q'(2a_4(\eta, 0) + 8\eta) + 4(\eta^2 + a_4(\eta, 0))} \tag{2.12}$$

at 3PN order where

$$a_4(\eta, \tilde{z}_1) = \left[\frac{94}{3} - \frac{41}{32}\pi^2 - \tilde{z}_1\right]\eta. \tag{2.13}$$

C. Adding spin couplings

There are several ways of including spin effects in the Hamiltonian dynamics. When considering the PN-expanded form of the orbital Hamiltonian $H^0_{\rm EXP}$, it is natural to add the spin-dependent terms as further additional contributions: $H_{\rm TOT} = H^0_{\rm EXP} + H^{\rm SPIN}$. On the other hand, when considering the EOB-resummed form of the Hamiltonian $H^0_{\rm EOB}$, it has been argued in Ref. [5] that it is probably better to incorporate most of the spin effects within a suitably generalized (à la Kerr) EOB Hamiltonian, whose explicit form will be found in [5]. In the present work, we shall, for technical simplicity, adopt a uniform way of including spin effects. Namely, we shall simply include them as linearly added contributions to the basic (PN-expanded or EOB-resummed) orbital Hamiltonian. We shall verify below that, in the EOB-resummed case, the two different ways (à la [5], or as in the following equation) of incorporating spin effects lead to very similar physical effects.

Finally, the explicit forms we shall use of the "spinning" Hamiltonian read

$$H_{\rm EXP}(\boldsymbol{X}, \boldsymbol{P}, \boldsymbol{S}_1, \boldsymbol{S}_2) = H^0_{\rm EXP}(\boldsymbol{X}, \boldsymbol{P}) + H_{\rm SO}(\boldsymbol{X}, \boldsymbol{P}, \boldsymbol{S}_1, \boldsymbol{S}_2) + H_{\rm SS}(\boldsymbol{X}, \boldsymbol{P}, \boldsymbol{S}_1, \boldsymbol{S}_2) \tag{2.14}$$

or

$$H_{\rm EOB}(\boldsymbol{X}, \boldsymbol{P}, \boldsymbol{S}_1, \boldsymbol{S}_2) = H^0_{\rm EOB}(\boldsymbol{X}, \boldsymbol{P}) + H_{\rm SO}(\boldsymbol{X}, \boldsymbol{P}, \boldsymbol{S}_1, \boldsymbol{S}_2) + H_{\rm SS}(\boldsymbol{X}, \boldsymbol{P}, \boldsymbol{S}_1, \boldsymbol{S}_2), \tag{2.15}$$

where [30,38,39]

$$H_{\rm SO} = 2\frac{\boldsymbol{S}_{\rm eff}.\boldsymbol{L}}{R^3}, \qquad \boldsymbol{S}_{\rm eff} \equiv \left(1 + \frac{3}{4}\frac{m_2}{m_1}\right)\boldsymbol{S}_1 + \left(1 + \frac{3}{4}\frac{m_1}{m_2}\right)\boldsymbol{S}_2, \tag{2.16}$$

$$H_{SS} = H_{S_1S_1} + H_{S_1S_2} + H_{S_2S_2} = \frac{1}{2R^3}\frac{\mu}{M}[3(\boldsymbol{S}_0 \cdot \boldsymbol{N})(\boldsymbol{S}_0 \cdot \boldsymbol{N}) - (\boldsymbol{S}_0 \cdot \boldsymbol{S}_0)], \tag{2.17}$$

$$\boldsymbol{S}_0 = \left(1 + \frac{m_2}{m_1}\right)\boldsymbol{S}_1 + \left(1 + \frac{m_1}{m_2}\right)\boldsymbol{S}_2, \tag{2.18}$$

$$H_{S_1S_2} = \frac{1}{R^3}[3(\boldsymbol{S}_1 \cdot \boldsymbol{N})(\boldsymbol{S}_2 \cdot \boldsymbol{N}) - (\boldsymbol{S}_1 \cdot \boldsymbol{S}_2)], \tag{2.19}$$

$$H_{S_1S_1} + H_{S_2S_2} = \frac{1}{2R^3}[3(\boldsymbol{S}_1 \cdot \boldsymbol{N})(\boldsymbol{S}_1 \cdot \boldsymbol{N}) - (\boldsymbol{S}_1 \cdot \boldsymbol{S}_1)]\frac{m_2}{m_1} + \frac{1}{2R^3}[3(\boldsymbol{S}_2 \cdot \boldsymbol{N})(\boldsymbol{S}_2 \cdot \boldsymbol{N}) - (\boldsymbol{S}_2 \cdot \boldsymbol{S}_2)]\frac{m_1}{m_2}, \tag{2.20}$$

with $\boldsymbol{N} = \boldsymbol{X}/R$, $R = |\boldsymbol{X}|$, and $\boldsymbol{L} = \boldsymbol{X} \times \boldsymbol{P}$. The spin-spin term $H_{S_1S_2}$ was derived in Ref. [39], while the spin-spin terms $H_{S_1S_1}$, $H_{S_2S_2}$, which are valid *only* for a BH binary, were derived in Ref. [5] [see the discussion around Eqs. (2.51)–(2.55) in Ref. [5] and also Ref. [32]]. They originate from the interaction of the monopole m_2 with the spin-induced quadrupole moment of the spinning black hole of mass m_1 and vice versa. The spin-induced quadrupole moment of a NS depends on the equation of state. So, if we were applying our approach to NS binaries, we could take into account the monopole-quadrupole interaction by multiplying $H_{S_1S_1}$, $H_{S_2S_2}$ by some equation-of-state-dependent coefficient γ (see Ref. [32]).

[1] As shown in [21], the use of the straightforward PN-expanded, 3PN-*accurate* "effective potential" $A(q')$ does not lead to a well-defined last stable circular orbit (contrary to what happens in the 2PN-accurate case [6]). This is due to the rather large value of the 3PN coefficient $\frac{94}{3} - \frac{41}{32}\pi^2 \simeq 18.688$ entering the PN expansion of $A(q')$. Replacing the PN-expanded form of $A(q')$ by a Padé approximant cures this problem. A comparison between the physical consequences of various possible resummations of $A(q')$ can be found in Ref. [23].

D. Equations of motion and conserved quantities

The time evolution of any dynamical quantity $f(\boldsymbol{X}, \boldsymbol{P}, \boldsymbol{S}_1, \boldsymbol{S}_2)$ is given by [5]

$$\frac{d}{dt} f(\boldsymbol{X}, \boldsymbol{P}, \boldsymbol{S}_1, \boldsymbol{S}_2) = \{f, H\}, \tag{2.21}$$

where with $\{\ldots,\ldots\}$ we indicated the Poisson brackets $\{X^i, P_j\} = \delta^i_j$. The Hamilton equations of motion are

$$\frac{d\boldsymbol{X}}{dt} = +\frac{\partial H}{\partial \boldsymbol{P}}, \qquad \frac{d\boldsymbol{P}}{dt} = -\frac{\partial H}{\partial \boldsymbol{X}}. \tag{2.22}$$

The equations of motion for the spins are easily derived as [5,39,40]

$$\frac{d}{dt}\boldsymbol{S}_1 = \{\boldsymbol{S}_1, H\} = \frac{\partial H}{\partial \boldsymbol{S}_1} \times \boldsymbol{S}_1 = \boldsymbol{\Omega}_1 \times \boldsymbol{S}_1, \tag{2.23}$$

$$\frac{d}{dt}\boldsymbol{S}_2 = \{\boldsymbol{S}_2, H\} = \frac{\partial H}{\partial \boldsymbol{S}_2} \times \boldsymbol{S}_2 = \boldsymbol{\Omega}_2 \times \boldsymbol{S}_2, \tag{2.24}$$

with

$$\boldsymbol{\Omega}_1 = \left(2 + \frac{3}{2}\frac{m_2}{m_1}\right)\frac{\boldsymbol{L}}{R^3} + \frac{1}{R^3}[3\boldsymbol{N}(\boldsymbol{S}_2 \cdot \boldsymbol{N}) - \boldsymbol{S}_2] + \frac{3}{R^3}\frac{m_2}{m_1}\boldsymbol{N}(\boldsymbol{S}_1 \cdot \boldsymbol{N}), \tag{2.25}$$

$$\boldsymbol{\Omega}_2 = \left(2 + \frac{3}{2}\frac{m_1}{m_2}\right)\frac{\boldsymbol{L}}{R^3} + \frac{1}{R^3}[3\boldsymbol{N}(\boldsymbol{S}_1 \cdot \boldsymbol{N}) - \boldsymbol{S}_1] + \frac{3}{R^3}\frac{m_1}{m_2}\boldsymbol{N}(\boldsymbol{S}_2 \cdot \boldsymbol{N}). \tag{2.26}$$

Note that a consequence of the above spin-evolution equations is the constancy of the lengths of the spin vectors: $\boldsymbol{S}_1^2 =$ cst., $\boldsymbol{S}_2^2 =$ cst.

When using the EOB Hamiltonian equation (2.15) we should, in principle, consider the canonical transformation between $(\boldsymbol{X}, \boldsymbol{P})$ and $(\boldsymbol{X}', \boldsymbol{P}')$ [6,21]. However, since the Hamilton equations are valid in any canonical coordinate system, when we evolve the EOB dynamics we write the Hamilton equations in terms of $(\boldsymbol{X}', \boldsymbol{P}')$ and for the spinning part we neglect the differences between $(\boldsymbol{X}', \boldsymbol{P}')$ and $(\boldsymbol{X}, \boldsymbol{P})$ which are of higher PN order. When in the following sections we compare the results between PN-expanded and PN-resummed Hamiltonians, we will always compare quantities which are gauge invariant to lowest order.

One of the advantages of using a Hamiltonian formalism is that one can immediately derive from the fundamental symmetries of the relative dynamics (time translation and spatial rotations) two *exact* conservation laws: that of the total energy $E = H$, and that of the total angular momentum $\boldsymbol{J} = \boldsymbol{L} + \boldsymbol{S}_1 + \boldsymbol{S}_2$. Using Eqs. (2.23) and (2.24) it is easy to check the conservation of the total energy,

$$\frac{dH}{dt} = \frac{\partial H}{\partial \boldsymbol{X}}\frac{d\boldsymbol{X}}{dt} + \frac{\partial H}{\partial \boldsymbol{P}}\frac{d\boldsymbol{P}}{dt} + \frac{\partial H}{\partial \boldsymbol{S}_1}\frac{d\boldsymbol{S}_1}{dt} + \frac{\partial H}{\partial \boldsymbol{S}_2}\frac{d\boldsymbol{S}_2}{dt} = 0. \tag{2.27}$$

Similarly, one easily checks the conservation of the total angular momentum $\boldsymbol{J} = \boldsymbol{L} + \boldsymbol{S}_1 + \boldsymbol{S}_2$. Note the remarkable fact that the orbital contribution to $\boldsymbol{J}$ is exactly given, at any PN order, by the "Newtonian-looking" expression $\boldsymbol{L} = \boldsymbol{X} \times \boldsymbol{P}$. This is contrary to what happens when working within a Lagrangian formalism, where the expression for the conserved orbital angular momentum gets modified at each PN order: $\boldsymbol{L} = \mu \boldsymbol{X} \times \boldsymbol{V} + O(c^{-2})$. Here, all the needed PN contributions are included in the Hamiltonian H (and thereby imply that $\boldsymbol{V} = \partial H/\partial \boldsymbol{P}$ is a complicated function of $\boldsymbol{V}$).

E. Spin-orbit interaction and "spherical orbits"

For most of the dynamical evolution, the spin-spin terms are much smaller than the spin-orbit ones. If we restrict ourselves to spin-orbit interactions, the equation of motion for the orbital angular momentum reads

$$\frac{d\mathbf{L}}{dt} = \{\mathbf{L}, H\} = \frac{2}{R^3}\mathbf{S}_{\rm eff} \times \mathbf{L}. \tag{2.28}$$

A useful consequence of this approximate evolution law is that $\boldsymbol{L}2$ is conserved. Under the same approximation, the total spin $\boldsymbol{S} = \boldsymbol{S}_1 + \boldsymbol{S}_2$ satisfies the equation

$$\frac{d\boldsymbol{S}}{dt} = -\frac{2}{R^3}\boldsymbol{S}_{\rm eff} \times \boldsymbol{L}. \tag{2.29}$$

The above (approximate) evolution equations exhibit clearly the (exact) conservation of the total angular momentum $\boldsymbol{J} = \boldsymbol{L} + \boldsymbol{S}$ ($d\boldsymbol{J}/dt = 0$).

It is also easily checked that $\boldsymbol{S}_{\rm eff} \cdot \boldsymbol{L}$ is a conserved quantity under the above, approximate evolution equations. Therefore, as emphasized by Damour [5], when only spin-orbit terms are included the orbital dynamics can be reduced to a simple "radial Hamiltonian" $H(R, P_R) = H(R, P_R, \boldsymbol{L}^2 = \text{const.}, \boldsymbol{S}_{\rm eff} \cdot \boldsymbol{L} = \text{const.})$ describing the radial motion. Here $P_R \equiv N^i P_i$ is the momentum canonically conjugated to R ($\{R, P_R\} = 1$). In this case there exists a class of *spherical orbits* satisfying

$$R = \text{const.}, \qquad P_R = 0, \qquad \frac{\partial H(R, P_R = 0, \boldsymbol{L}^2, \boldsymbol{L} \cdot \boldsymbol{S}_{\rm eff})}{\partial R} = 0. \tag{2.30}$$

F. Characteristics of the last stable spherical orbit

When spin-spin interactions are included, those spherical orbits no longer exist as exact solutions. However, as spin-spin effects are always smaller than spin-orbit ones, one expects that the above *spherical* orbits will play the same important role as the usual *circular* orbits in the nonspinning case. In particular, the *last stable spherical*

orbit (LSSO) should play the important role of delineating the transition between adiabatic inspiral and plunge.

The LSSO for the spinning conservative dynamics is determined by setting

$$\frac{\partial H_0}{\partial R} = 0 = \frac{\partial^2 H_0}{\partial R^2}, \tag{2.31}$$

where $H_0(R, P_R, P_\phi, \ldots) = H(R, 0, P_\phi, \ldots)$.

The physical characteristics of the LSSO for (aligned or antialigned) spinning configurations were studied in detail in Ref. [5] within the more fully resummed Kerr-like EOB Hamiltonian introduced in that reference. It was also shown in [23] that the predictions from the latter Kerr-like EOB Hamiltonian were in good agreement with the numerical results on corotating BH binaries obtained by means of the helical Killing vector approach [24] (see, e.g., Table I of [23] and [41,42]). (Note that the agreement with EOB is better when one considers the 3PN accuracy.) Except for corotating configurations, all the currently published numerical estimates of the physical characteristics of close binaries made of *spinning* BH's (such as [43]) use the conformal-imaging formalism rather than the physically better motivated HKV one. For this reason we shall not try to compare here the analytical EOB predictions for spinning configurations with numerical results. On the other hand, it is interesting to compare several different, PN-rooted, analytical approaches in their predictions for the binding energy of close BH binaries.

The most straightforward PN-based analytical approach to the physical characteristics of close BH binaries consists of starting from the fully PN-expanded Hamiltonian (2.14), considered as defining an exact dynamics, and then to deduce from it the energy and angular frequency of spherical orbits. [We consider here only configurations where the spins are parallel (or antiparallel) to the orbital angular momentum, so that it makes sense, even in the presence of spin-spin interactions, to consider spherical (and actually circular) orbits.] The binding energy of such "PN-expanded" spherical orbits is plotted in the left panel of Fig. 1 as a function of the orbital angular frequency, for equal-mass BH binaries. As we see from this figure, the straightforward PN-expanded Hamiltonian does not exhibit any minimum of the binding energy, i.e. it does not lead to any LSSO in the nonspinning or aligned maximally spinning cases. As the best current numerical results on BH binaries clearly indicate the existence of such LSSO's, this disqualifies the use of the fully PN-expanded Hamiltonian (2.14) for describing close binaries.

It has, however, been pointed out [44] that more reasonable results, close to the numerical HKV results, can be obtained by plotting, instead of the prediction coming straightforwardly from (2.14), the PN expansion of the analytically computed function $E(\Omega)$ giving the binding energy E as a function of the orbital frequency Ω. Indeed, one can derive from (2.14) the following explicit PN expansion of the (invariant) function $E(\Omega)$ [21,44,45]:

$$\begin{aligned} E_{\rm 2PN}(\Omega) = -\frac{\mu}{2}(M\Omega)^{2/3}\Big\{1 - \frac{(9+\eta)}{12}(M\Omega)^{2/3} \\ + \frac{8}{3}\frac{\hat{\boldsymbol{L}}\cdot\boldsymbol{S}_{\rm eff}}{M^2}(M\Omega) \\ + \frac{1}{24}(-81 + 57\eta - \eta^2)(M\Omega)^{4/3} \\ + \frac{1}{\eta}\frac{1}{M^4}[\boldsymbol{S}_1\cdot\boldsymbol{S}_2 - 3(\hat{\boldsymbol{L}}\cdot\boldsymbol{S}_1)(\hat{\boldsymbol{L}}\cdot\boldsymbol{S}_2)] \\ \times (M\Omega)^{4/3}\Big\}, \end{aligned} \tag{2.32}$$

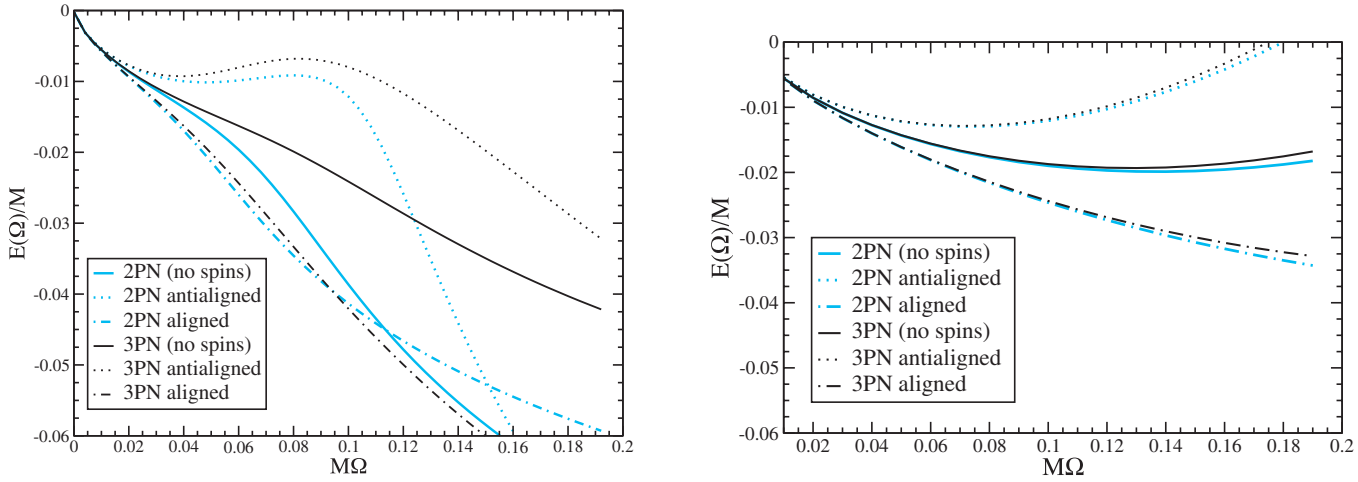

FIG. 1 (color online). The energy for circular orbits as a function of the frequency evaluated using the PN-expanded Hamiltonian (left panel) and the PN expansion of the analytically computed function given by Eq. (2.32) (right panel) at various PN orders for maximal spins and equal-mass binaries.

$$E_{3\mathrm{PN}}(\Omega) = E_{2\mathrm{PN}}(\Omega) - \frac{\mu}{2}(M\Omega)^{2/3}\left\{\left[-\frac{675}{64} + \left(\frac{34\,445}{576} - \frac{205}{96}\pi^2\right)\eta - \frac{155}{96}\eta^2 - \frac{35}{5184}\eta^3\right](M\Omega)^2\right\}. \tag{2.33}$$

These functions are plotted in the right panel of Fig. 1. Visibly, they are much better behaved than the results plotted in the left panel, which came directly from the PN-expanded Hamiltonian. They are also close to the numerical HKV results [44]. The fact that two expressions, which can both be called PN-expanded, and which are supposedly equivalent "modulo higher PN terms," lead to physically markedly different results leads us to conclude that the PN-expanded Hamiltonian cannot be used to describe the transition from adiabatic inspiral to plunge. Let us also recall that if we consider, in the absence of spins, the test-mass limit $\eta \to 0$, instead of the equal-mass one $\eta \to 1/4$, the PN expansions (2.32) and (2.33) have been shown (see [21]) to be quite inaccurate representations of the known exact expression of the function $E(\Omega)$. Indeed, the 2PN-accurate function (2.32) predicts in this limit a LSO frequency which is 82% larger than the exact one, while the 3PN-accurate one (2.33) predicts a LSO frequency 27% larger than the exact one.

By contrast with these problematic features of PN-expanded results,[2] the EOB approach leads to uniformly better behaved results (even if we use it not in the Kerr-like form advocated in [5], but in the form (2.15) used in the present paper). We show in Fig. 2 the EOB analog of Fig. 1, i.e. the function $E(\Omega)$ deduced from the EOB Hamiltonian (2.15) in the aligned, antialigned, and nonspinning cases. In this EOB case, we have none of the problems entailed by the PN-expanded approach, and the uniquely defined curve $E(\Omega)$ was shown in [23] to agree well with the HKV numerically determined curve (for corotating holes). Note, however, that *aligned* maximally rotating holes lead to a curve which, especially in the 3PN case, reaches a minimum (not shown on Fig. 2) only for a rather high angular velocity.

This property of the aligned configurations (as well as the significant difference between the 2PN-EOB result and the 3PN-EOB one) was already emphasized in [5]. As it will be important for the present paper, we study it further by plotting in Fig. 3 the dependence on the $\boldsymbol{L}$-projected effective spin parameter

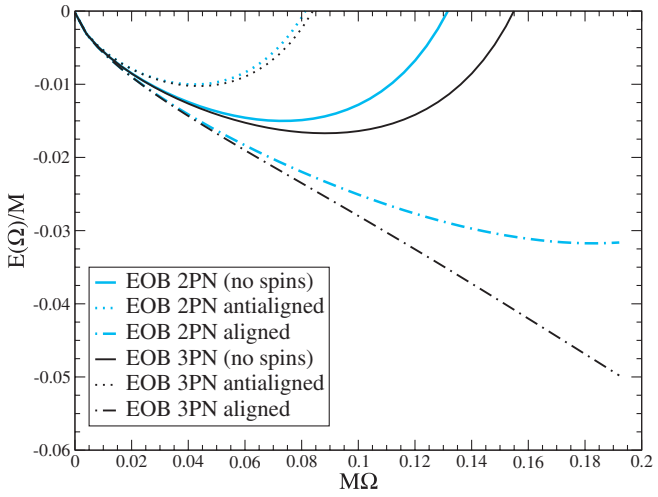

FIG. 2 (color online). The energy for circular orbits as a function of the frequency evaluated from the EOB Hamiltonian at various PN orders for maximal spins and equal-mass binaries.

$$\chi_L \equiv \frac{\boldsymbol{S}_{\mathrm{eff}} \cdot \hat{\boldsymbol{L}}}{M^2} \tag{2.34}$$

[where $\boldsymbol{S}_{\mathrm{eff}}$ was defined in Eq. (2.16) above] of the binding energy E and the angular frequency Ω *at the LSSO*, i.e. at the minimum of the $E(\Omega)$ curve. The first four curves in this figure show four results obtained for equal-mass and equal-spin configurations within the EOB approach: (i) the result obtained from the Hamiltonian (2.15) when using the 2PN-accurate orbital EOB Hamiltonian, (ii) the result obtained from (2.15) when using the 3PN-accurate orbital EOB Hamiltonian, (iii) the result obtained from the 2PN-accurate Kerr-like Hamiltonian introduced in [5], and (iv) the result obtained from the 3PN-accurate Kerr-like Hamiltonian introduced in [5]. (The latter two Hamiltonians are referred to in the caption as "SO Resummed," because they include a resummation à la EOB of the spin-orbit interactions.) In addition, as we cannot show on this plot the minimum of the $E(\Omega)$ curve deduced from the PN-expanded Hamiltonian, because the left panel of Fig. 1 shows that it does not exist, we show instead, for comparison purposes, the characteristics of the minimum of the PN-expanded functions (2.32) and (2.33) (i.e. the right panel of Fig. 1).

It is interesting to note in Fig. 3 that the effect of resumming (à la Kerr) or not the spin-orbit interaction seems to be rather small. We see also that, when considering antialigned configurations, all calculations give very similar results. This is not surprising as the *attractive* ($H_{\mathrm{SO}} < 0$) nature of the *antialigned* spin-orbit (and spin-spin) interaction has the effect of pushing the LSSO *outwards*, i.e. toward larger-radius, lower-frequency, less bound and therefore less relativistic configurations. On the other hand, working at the 2PN or the 3PN level induces, as already pointed out in [5], a very significant

[2]Let us recall here that, in order to be able to describe the transition between inspiral and plunge, we cannot use just the function $E(\Omega)$, but we need a full description of the binary dynamics. Therefore, if we wanted to confine ourselves to a PN-expanded approach, we would have to use either the PN-expanded Hamiltonian (2.14), or the corresponding (appropriately truncated) PN-expanded equations of motion. The left panel of Fig. 1 shows that this would not be a reliable thing to do. This is also clear from some of the results of Ref. [25].

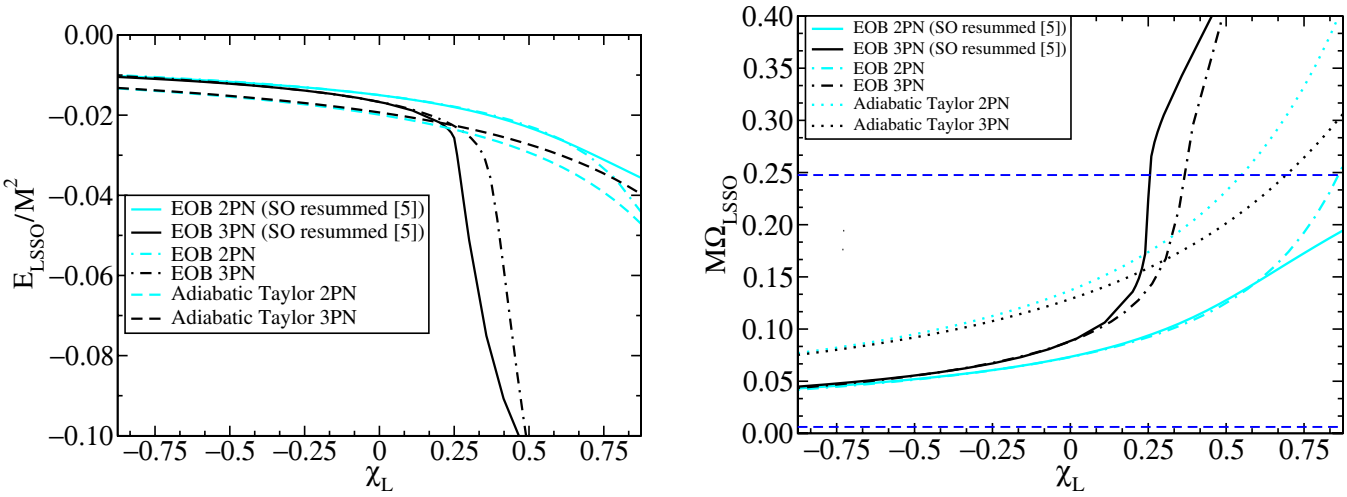

FIG. 3 (color online). The energy (left panel) and the frequency (right panel) at the LSSO as a function of $\chi_L \equiv S_{\rm eff} \cdot \hat{L}/M^2$ in the equal-mass case for the EOB Hamiltonian and PN-expanded, analytically computed function $E(\Omega)$ (see right panel of Fig. 1). The horizontal dashed line in the right panel marks the highest LSSO angular frequency for BBHs with total mass in the range 10–40$M_\odot$, assuming the LIGO frequency band $40 \leq f_{\rm GW} \leq 240$ Hz.

difference for the LSSO characteristics in the *aligned* case (positive χ_L). In this case, because of the *repulsive* ($H_{\rm SO} > 0$) nature of the *aligned* spin-orbit (and spin-spin) interaction, the LSSO is drawn towards closer, higher-frequency, more bound and more relativistic configurations. For such very compact configurations the *repulsive* sign ($a_4 > 0$) of the 3PN contribution to the effective potential $A(q)$ further amplifies, by a "snowball effect," the tendency toward closer and more bound configurations. We think that this could be a physically real effect due (as confirmed independently by Refs. [46,47]) to the large positive value of the crucial 3PN coefficient entering a_4, Eq. (2.13). This large positive value for a_4 is also needed to improve (with respect to the 2PN case) the agreement between the HKV corotating results and the 3PN-EOB ones [23]. It would be interesting to have numerical HKV studies of the LSSO for moderately- and fast-spinning aligned BH's to test the predictions made by the EOB approach. [Numerical results of the initial-value problem of Ref. [43], which extend up to mildly positive values of $\chi_L \sim 0.17$, are in rough qualitative agreement (especially for the dependence of $\Omega_{\rm LSSO}$ on χ_L) with the EOB predictions, but their quantitative agreement is too poor to reach a firm conclusion.]

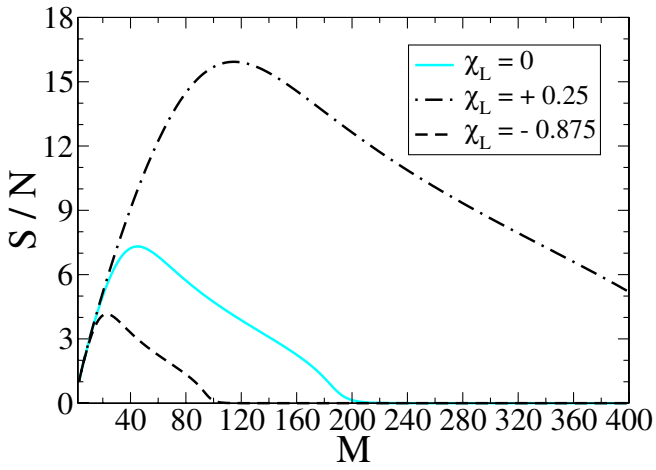

FIG. 4 (color online). Signal-to-noise ratio versus binary total mass at 100 Mpc for equal-mass binaries with LSSO determined by the 3PN-EOB Hamiltonian.

Let us note in passing that the significant dependence of the LSSO frequency on the effective spin parameter χ_L makes it desirable for data-analysis purposes, when one is content with using adiabatic templates [15], to use at least templates whose ending frequency is not fixed, say, to the usually considered Schwarzschild LSO, but varies with masses and spins as suggested by the EOB approach.

Finally, another consequence of the significant dependence of the LSSO frequency on the effective spin parameter χ_L is drawn in Fig. 4, where we compare the signal-to-noise ratios (SNRs) as a function of the binary total mass for an optimally oriented equal-mass binary at 100 Mpc. We use the LIGO design sensitivity noise curve [19]. The SNRs are obtained observing the inspiral from 40 Hz until the LSSO predicted by the EOB approach at 3PN order. The three curves refer to nonspinning binaries and binaries with $\chi_L = -0.875, 0.25$. Figure 4 reveals a bias towards first detecting mostly aligned spinning binaries with high masses, as pointed out in [5].

III. RADIATION REACTION, INCLUDING SPIN EFFECTS

The previous section has reviewed various ways of describing the conservative dynamics of binary systems (including spin effects). In the present section, we discuss the inclusion of radiation-reaction effects, with emphasis

on determining the spin modifications of radiation reaction. Within the Hamiltonian approach, that we use here, radiation reaction can be incorporated by modifying the usual Hamilton equations in the following way:

$$\frac{dX^i}{dt} = \{X^i, H\} = \frac{\partial H}{\partial P_i},$$
$$\frac{dP_i}{dt} = \{P_i, H\} + F_i = -\frac{\partial H}{\partial X^i} + F_i. \tag{3.1}$$

Here, F_i denotes a "nonconservative force," which is added to the evolution equation of the (relative) momentum to take into account RR effects. This RR force $\boldsymbol{F}$ depends, *a priori*, both on the (relative) orbital variables $\boldsymbol{X}, \boldsymbol{P}$ and on the spin variables $\boldsymbol{S}_1, \boldsymbol{S}_2$. In the present paper, our aim will be limited to determining F_i under the following two simplifying assumptions: (i) we consider only *quasicircular orbits*, and (ii) we shall retain only the *leading spin-dependent terms*. After the completion of the work reported in this section, there appeared a work by Will [33] dealing with spin-dependent, radiation-reaction effects in general orbits. As the derivations are not the same, and yield results which we have checked to be equivalent (for circular orbits), but expressed in different variables (Hamiltonian $\boldsymbol{X}, \boldsymbol{P}$ here vs Lagrangian $\boldsymbol{X}, \boldsymbol{V}$ for [33]), we feel it worth briefly reporting our derivation.

Because of assumption (ii), we look for terms in F_i which are *linear* in the spin tensors $S^a_{ij} \equiv \varepsilon_{ijk} S^k_a$ ($a = 1, 2$) of the two considered compact bodies. (Note that spin effects enter the metric only through the spin tensors S^a_{ij}, rather than through the axial spin vectors S^k_a.) As the time derivative of S^a_{ij} contains a "small" post-Newtonian factor G/c^2, the leading spin-dependent terms in F_i will contain only the undifferentiated spin tensors.

Using Euclidean invariance, the spin-dependent terms in the force $F_i(\boldsymbol{X}, \boldsymbol{P}, \boldsymbol{S}_a)$ must be a combination of three types of contributions: $c_1 S_{ij} X^j$, $c_2 S_{ij} P^j$, and $c_i S_{jk} X^j P^k$, where $c_1(\boldsymbol{X}, \boldsymbol{P})$, $c_2(\boldsymbol{X}, \boldsymbol{P})$ are some scalar functions of $\boldsymbol{X}, \boldsymbol{P}$, while c_i is a vector function of $\boldsymbol{X}, \boldsymbol{P}$. (Here, S_{ij} denotes one of the two spin vectors. We shall sum over the two possible spins at the end.) Imposing that the radiation-reaction force F_i be *odd under time reversal*, i.e. odd under the simultaneous changes $X^i \to X^i$, $P_i \to -P_i$, $S_{ij} \to -S_{ij}$, tells us that $c_1(\boldsymbol{X}, \boldsymbol{P})$ must be an *even* function of $\boldsymbol{P}$, $c_2(\boldsymbol{X}, \boldsymbol{P})$ must be an *odd* function of $\boldsymbol{P}$, and the vector $c_i(\boldsymbol{X}, \boldsymbol{P})$ must be an *odd* function of $\boldsymbol{P}$. (Note also that c_i must be a true vector, not an axial vector. By parity invariance no ε_{ijk} can appear, except in combination with S^k_a.) Therefore, if we further decompose $c_i = c_3(\boldsymbol{X}, \boldsymbol{P}) P_i + c_4(\boldsymbol{X}, \boldsymbol{P}) X_i$, the coefficient $c_3(\boldsymbol{X}, \boldsymbol{P})$ must be *even* in $\boldsymbol{P}$, while the coefficient $c_4(\boldsymbol{X}, \boldsymbol{P})$ must be *odd* in $\boldsymbol{P}$.

At this point, our simplifying assumption (i) above (quasicircular motion) will bring a drastic simplification. Indeed, a time-odd scalar must contain an odd power of the combination $X^k P_k$. However, this combination vanishes along circular orbits (and is therefore subleadingly small along adiabatically inspiraling orbits). To leading order the scalar coefficients c_2 and c_4 therefore vanish, and we conclude that F_i contains only two independent spin contributions: $c_1(\boldsymbol{X}, \boldsymbol{P}) S_{ij} X^j + c_3(\boldsymbol{X}, \boldsymbol{P}) P_i S_{jk} X^j P^k$. It will be convenient in the following to further decompose the vector $S_{ij} X^j$ entering the first contribution (which is orthogonal to X^i) into its component along the direction of P_i, and its component orthogonal to P_i, say

$$(S_{ij} X^j)^\perp \equiv (\delta_{ik} - P_i P_k / \boldsymbol{P}^2) S_{kj} X^j = S_{ij} X^j + \frac{P_i}{\boldsymbol{P}^2} S_{jk} X^j P^k. \tag{3.2}$$

It is easily checked that, along circular orbits ($X^i P_i = 0$), the vector (3.2) is orthogonal *both* to $\boldsymbol{P}$ and to $\boldsymbol{X}$. Therefore, $(S_{ij} X^j)^\perp$ is parallel to the orbital angular-momentum (axial) vector

$$L_i \equiv \varepsilon_{ijk} X^j P_k. \tag{3.3}$$

It is easily checked that

$$(S_{ij} X^j)^\perp = \frac{R^2}{\boldsymbol{L}^2} (\boldsymbol{P} \cdot \boldsymbol{S}) L_i = \frac{1}{\boldsymbol{P}^2} (\boldsymbol{P} \cdot \boldsymbol{S}) L_i. \tag{3.4}$$

Finally, adding the usual spin-independent radiation reaction (parallel to P_i for circular orbits), and summing over the two bodies, we conclude that the RR force can be written as

$$F_i(\boldsymbol{X}, \boldsymbol{P}, \boldsymbol{S}_a) = B P_i + \sum_{a=1,2} A_a (S^a_{ij} X^j)^\perp$$
$$= B P_i + \sum_{a=1,2} \frac{A_a}{\boldsymbol{P}^2} (\boldsymbol{P} \cdot \boldsymbol{S}_a) L_i, \tag{3.5}$$

with

$$B \equiv B_0 + \sum_{a=1,2} C_a S^a_{jk} X^j P^k = B_0 + \sum_{a=1,2} C_a \boldsymbol{L} \cdot \boldsymbol{S}_a, \tag{3.6}$$

where B_0, C_a, and A_a are some time-even functions of $\boldsymbol{X}$ and $\boldsymbol{P}$.

To determine the coefficients B_0, C_a, and A_a, we now impose that there be a balance between the losses of mechanical energy and angular momentum of the system due to the additional force F_i in the Hamilton equations of motion (3.1) and the losses of energy and angular momentum at infinity due to the emission of gravitational radiation. Let us first recall that, in the Hamiltonian formalism, the quantities

$$E(t) \equiv H(\boldsymbol{X}(t), \boldsymbol{P}(t), \boldsymbol{S}_a(t)),$$
$$J_{ij}(t) \equiv X^i P_j - X^j P_i + S^1_{ij} + S^2_{ij} \tag{3.7}$$

are exact constants of the motion in absence of RR force in Eqs. (3.1) and in the Hamiltonian equations for spin evolution. When adding the RR force $\boldsymbol{F}$ in Eqs. (3.1) (and no corresponding RR torque in the spin-evolution equations)

we find that E and $\boldsymbol{J}$ evolve as

$$\frac{dE}{dt} = \frac{\partial H}{\partial P_i} F_i = \dot{X}^i F_i, \tag{3.8}$$

$$\frac{dJ_{ij}}{dt} = X^i F_j - X^j F_i. \tag{3.9}$$

Inserting in Eqs. (3.8) and (3.9) the expression (3.5) for the RR force F_i, we can easily evaluate the *averaged* losses of energy and angular momentum. Along (quasi) circular orbits, the various scalar coefficients B_0, C_a, A_a are time independent (because all basic scalars, $\boldsymbol{X}^2$, $\boldsymbol{P}^2$, $\boldsymbol{X}\cdot\boldsymbol{P} = 0$, are constant). One then finds that dE/dt is time independent, while dJ_{ij}/dt depends on the orbital phase only in spin-dependent terms and through the tensor $X^i P_j$. Decomposing the latter tensor into

$$\begin{aligned} X^i P_j &= \frac{1}{2}(X^i P_j + X^j P_i) + \frac{1}{2}(X^i P_j - X^j P_i) \\ &\simeq \frac{d}{dt}\left(\frac{1}{2}\mu X^i X^j\right) + \frac{1}{2} L_{ij}, \end{aligned} \tag{3.10}$$

one easily sees that its orbital average is simply $\langle X^i P_j\rangle = \frac{1}{2} L_{ij}$. (We consider averages over the orbital period, considering all more slowly evolving quantities, such as $\boldsymbol{L}$, as fixed during one orbital period.)

When evaluating Eq. (3.8) along circular orbits, we cannot use the Newtonian approximation $\dot{X}^i \simeq P^i/\mu$ because we wish to obtain the coefficient B with a high post-Newtonian accuracy. However, we can instead use $\dot{X}^i P_i = \dot{\phi} P_\phi = \omega |\boldsymbol{L}|$ where $\omega = \dot{\phi} = V/R$ denotes the orbital angular frequency. We finally obtain

$$\frac{dE}{dt} = B\omega |\boldsymbol{L}|, \tag{3.11}$$

$$\left\langle \frac{d\boldsymbol{J}}{dt} \right\rangle = B\boldsymbol{L} - \frac{1}{2}\sum_{a=1,2} A_a R^2 [\boldsymbol{S}_a - \boldsymbol{\lambda}(\boldsymbol{\lambda}\boldsymbol{S}_a)], \tag{3.12}$$

where $\boldsymbol{\lambda} \equiv \boldsymbol{L}/|\boldsymbol{L}|$ denotes the unit vector along the orbital angular momentum. Note that Eqs. (3.11) and (3.12) predict a link between energy loss and angular-momentum loss, namely

$$\frac{dE}{dt} = \omega \boldsymbol{\lambda} \cdot \left\langle \frac{d\boldsymbol{J}}{dt} \right\rangle. \tag{3.13}$$

To obtain the values of the coefficients B and A_a [and to test the prediction (3.13)], we need to compare Eqs. (3.11) and (3.12) with the values of the averaged fluxes of energy and angular momentum at infinity. The spin contributions to the latter losses have been computed by Kidder [9]. However, one must be careful with the fact that Kidder expressed most of his results in terms of *harmonic coordinates*, with the choice of a covariant spin supplementary condition: $S^a_{\mu\nu} u^\nu_a = 0$.

First, using the results of Ref. [9] as they are, one straightforwardly checks that the relation (3.13) is satisfied. This is a check that it is enough to include RR effects in the orbital equations of motion (3.1), without modifying the spin equations of motion. (For a direct dynamical check, see [33].) Then, to obtain the value of the coefficient B we can simply use the result (3.11), namely

$$B = \frac{1}{\omega |\boldsymbol{L}|} \frac{dE}{dt}, \tag{3.14}$$

where it remains to express dE/dt (computed as a flux at infinity, using Ref. [9]) in terms of our basic (Hamiltonian) dynamical variables. One way to proceed would be to transform the harmonic-coordinate results of [9] into ADM coordinates (with the corresponding spin condition $S_{i0} + \frac{1}{2} S_{ij} v^j = 0$ [30]). The transformation linking the two coordinates has been worked out in [30] for the spin-dependent terms and in [48,49] for the spin-independent parts. However, a simpler way to proceed is to eliminate references to specific coordinates by expressing dE/dt (for circular orbits) in terms of the gauge-invariant orbital frequency ω. Adding also, for better accuracy, the recently completed 3PN flux contribution [50–52], we have

$$\begin{aligned} \frac{dE}{dt} = -\frac{32}{5}\eta^2 v_\omega^{10} \{1 &+ f_2(\eta) v_\omega^2 + [f_3(\eta) + f_{3\mathrm{SO}}] v_\omega^3 \\ &+ [f_4(\eta) + f_{4\mathrm{SS}}] v_\omega^4 + f_5(\eta) v_\omega^5 + f_6(\eta) v_\omega^6 \\ &+ f_{\ell 6} v_\omega^6 \ln(4 v_\omega) + f_7(\eta) v_\omega^7\}, \end{aligned} \tag{3.15}$$

where $v_\omega \equiv (GM\omega)^{1/3}$, where the spin-independent flux coefficients $f_2(\eta), \ldots, f_7(\eta)$, are given by

$$f_2(\eta) = -\frac{1247}{336} - \frac{35}{12}\eta, \tag{3.16}$$

$$f_3(\eta) = 4\pi, \tag{3.17}$$

$$\begin{aligned} f_4(\eta) &= -\frac{44\,711}{9072} + \frac{9271}{504}\eta + \frac{65}{18}\eta^2, \\ f_5(\eta) &= -\left(\frac{8191}{672} + \frac{583}{24}\eta\right)\pi, \end{aligned} \tag{3.18}$$

$$\begin{aligned} f_6(\eta) = \frac{6\,643\,739\,519}{69\,854\,400} &+ \frac{16}{3}\pi^2 - \frac{1712}{105}\gamma_E \\ &+ \left(-\frac{134\,543}{7776} + \frac{41}{48}\pi^2\right)\eta - \frac{94\,403}{3024}\eta^2 - \frac{775}{324}\eta^3, \end{aligned} \tag{3.19}$$

$$f_{\ell 6} = -\frac{1712}{105}, \tag{3.20}$$

$$f_7(\eta) = \left(-\frac{16\,285}{504} + \frac{214\,745}{1728}\eta + \frac{193\,385}{3024}\eta^2\right)\pi, \tag{3.21}$$

with γ_E being Euler's gamma, and where the spin-dependent corrections to the latter flux coefficients are

$$f_{3\mathrm{SO}} = -\left(\frac{11}{4}+\frac{5}{4}\frac{m_2}{m_1}\right)\frac{\boldsymbol{\lambda}\cdot\boldsymbol{S}_1}{GM^2} - \left(\frac{11}{4}+\frac{5}{4}\frac{m_1}{m_2}\right)\frac{\boldsymbol{\lambda}\cdot\boldsymbol{S}_2}{GM^2}, \tag{3.22}$$

$$f_{4\mathrm{SS}} = \frac{\eta}{48G^2m_1^2m_2^2}[289(\boldsymbol{\lambda}\cdot\boldsymbol{S}_1)(\boldsymbol{\lambda}\cdot\boldsymbol{S}_2) - 103\boldsymbol{S}_1\cdot\boldsymbol{S}_2] + \mathcal{O}(\boldsymbol{S}_1^2) + \mathcal{O}(\boldsymbol{S}_2^2). \tag{3.23}$$

The present work was aimed at determining the leading spin-dependent terms, i.e. the ones linear in $\boldsymbol{S}_1$ and $\boldsymbol{S}_2$, as exemplified in the correction $f_{3\mathrm{SO}}$, Eq. (3.22), to the coefficient $f_3 = 4\pi$. For completeness, as the link (3.14) between the "longitudinal" part of RR, $F_i^{\mathrm{long}} = BP_i$, and the energy loss is clearly general, we have also used Kidder's results [9] to write down the part of B which depends on the product $\boldsymbol{S}_1^i\boldsymbol{S}_2^j$. The numerically similar contributions which depend on $\boldsymbol{S}_1^i\boldsymbol{S}_1^j$ and $\boldsymbol{S}_2^i\boldsymbol{S}_2^j$ have not yet been determined. Only partial results are known. For instance, Poisson [32] has derived a contribution to $f_{4\mathrm{SS}}$ of the form

$$\left[\frac{3(\boldsymbol{\lambda}\cdot\boldsymbol{S}_1)^2-\boldsymbol{S}_1^2}{G^2m_1^2M^2}+\frac{3(\boldsymbol{\lambda}\cdot\boldsymbol{S}_2)^2-\boldsymbol{S}_2^2}{G^2m_2^2M^2}\right], \tag{3.24}$$

but many other additional contributions $\mathcal{O}(\boldsymbol{S}_1^2)+\mathcal{O}(\boldsymbol{S}_2^2)$ have not yet been computed.

Let us finally turn to the determination of the other spin-related coefficients, A_a, in Eq. (3.12). Again, we have the technical problem that Ref. [9] expressed its results in terms of harmonic-coordinate quantities. Namely, Eq. (4.11) of Ref. [9] expresses the total angular-momentum loss $d\boldsymbol{J}/dt$ in terms of the harmonic distance r and of the harmonic-coordinate "Newtonian orbital momentum" $\boldsymbol{L}_N \equiv \mu\boldsymbol{x}\times\boldsymbol{v}$ (where $\boldsymbol{x}$ and $\boldsymbol{v}$ denote the relative harmonic position and velocity). A simple way to convert this result to our ADM distance R and our ADM total orbital momentum $\boldsymbol{L} \equiv \boldsymbol{X}\times\boldsymbol{P}$ is to relate $\boldsymbol{L}_N$ to $\boldsymbol{L}$ by comparing the expression (4.7) of Ref. [9] for the (gauge-invariant) conserved total angular momentum $\boldsymbol{J}$ with the corresponding simple ADM expression (3.7). This yields a result of the form

$$\hat{\boldsymbol{L}}_N \equiv \frac{\boldsymbol{L}_N}{|\boldsymbol{L}_N|} = c\boldsymbol{L} + \left(\frac{GM}{r}\right)^{3/2}\sum_{a=1,2}\chi_a\hat{\boldsymbol{s}}_a\left(\frac{m_a^2}{M^2}+\frac{1}{4}\eta\right), \tag{3.25}$$

where the coefficient c is not needed for our present purpose, and where, following the notation of [9], $\boldsymbol{S}_a \equiv \chi_a m_a^2\hat{\boldsymbol{s}}_a$. Inserting Eq. (3.25) in Eq. (4.11) of [9] allows one to compute easily the part of $d\boldsymbol{J}/dt$ which is proportional to the projection of $\boldsymbol{S}a$ orthogonally to $\boldsymbol{L}$.

This yields the following expression for the coefficients A_a in Eq. (3.5):

$$A_a = \frac{8}{15}\eta^2\frac{v_\omega^8}{R^3}\left(61+48\frac{m_{a'}}{m_a}\right), \tag{3.26}$$

where $a' \neq a$ (e.g. $a' = 2$ when $a = 1$). Summarizing, the radiation-reaction force to be added to the Hamiltonian equations of motion (3.1) reads

$$F_i = \frac{1}{\omega|\boldsymbol{L}|}\frac{dE}{dt}P_i + \frac{8}{15}\eta^2\frac{v_\omega^8}{\boldsymbol{L}^2R}\left\{\left(61+48\frac{m_2}{m_1}\right)\boldsymbol{P}\cdot\boldsymbol{S}_1 + \left(61+48\frac{m_1}{m_2}\right)\boldsymbol{P}\cdot\boldsymbol{S}_2\right\}L_i, \tag{3.27}$$

where the energy loss [expressed in terms of the orbital frequency ω, or equivalently of $v_\omega \equiv (GM\omega)^{1/3}$, and of the spin variables] is given by Eqs. (3.15), (3.16), (3.17), (3.18), (3.19), (3.20), (3.21), (3.22), and (3.23). We have checked that, after taking into account the relation between the Hamiltonian variables $\boldsymbol{X}, \boldsymbol{P}$ and the Lagrangian ones $\boldsymbol{X}, \boldsymbol{V}$ (which involves spin-dependent terms because of the first Eq. (2.22), Eq. (3.27) agrees with the circular limit of Eq. (1.6) of [33] (which assumes the same spin condition as we do).

References [7,19,22,53] have shown that (at least in the test-mass limit where one can compare analytical and numerical estimates) it is generally advantageous to replace the Taylor series in curly brackets on the right-hand side (R.H.S.) of Eq. (3.15) by its (suitably defined) Padé resummation. In particular, Porter and Sathyaprakash [53] have compared "Taylor" and "Padé" approximants for the flux function of a test particle around a Kerr black hole with the exact numerical estimates [54] and concluded that Padé approximants are, when considering all values of the spin parameter, both more *effectual* (i.e., larger overlaps with the exact signal) and more *faithful* (i.e., smaller biases in parameter estimates) than Taylor approximants. (We use here the terminology introduced in [19].) In view of this, and as was already advocated in [7], we consider that the best way to incorporate a radiation-reaction force in the EOB approach is to insert Padé approximants of the flux function [R.H.S. of (3.15)] in (3.27). However, for added generality, we shall also consider the case where we leave the flux function as a plain Taylor series. Note that, when considering arbitrary values of the dimensionless spin parameters for the two holes $\chi_1 \equiv S_1/Gm_1^2$, $\chi_2 \equiv S_2/Gm_2^2$, we used the normal "direct" (i.e., lower-diagonal) Padé approximants, instead of the "inverse" (i.e., upper-diagonal) ones used in [53]. For some values of the spin parameters, both the lower- and upper-diagonal Padé approximants have poles. When this occurs, we apply the Padé approximant only to the nonspinning part of the flux and add the spinning terms separately. There exist other Padé approximants in which poles are absent and it would be very desirable to determine them in the entire parameter space. This is beyond the scope of this paper.

In Figs. 5 and 6 we show T and (lower-diagonal) P approximants at 3.5PN order for an equal-mass binary

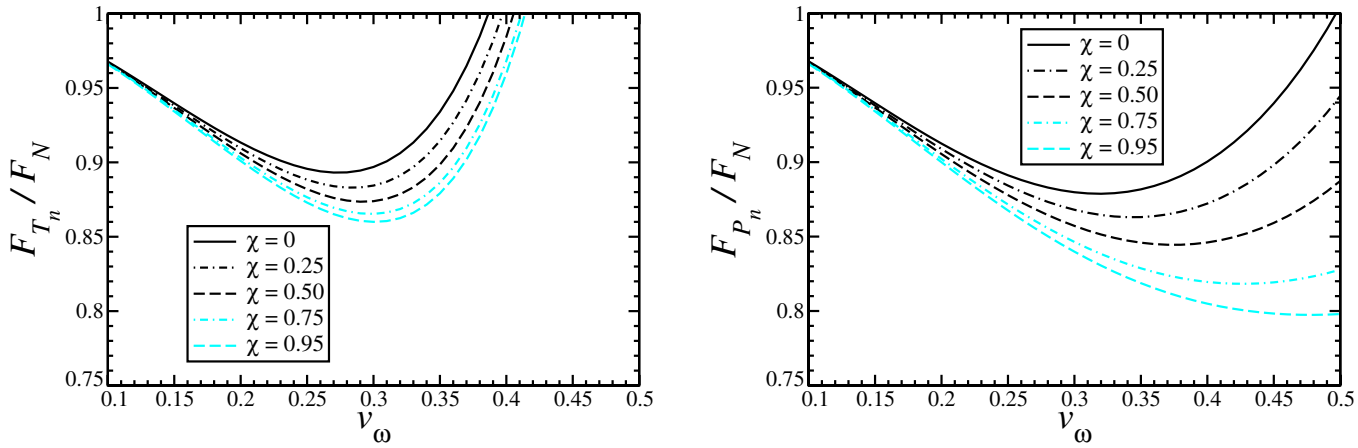

FIG. 5 (color online). Newton-normalized flux in the equal-mass case with both BH spins aligned (and maximal $\chi = \chi_1 = \chi_2$) with orbital angular momentum when T approximants (left panel) and (lower-diagonal) P approximants (right panel) are used.

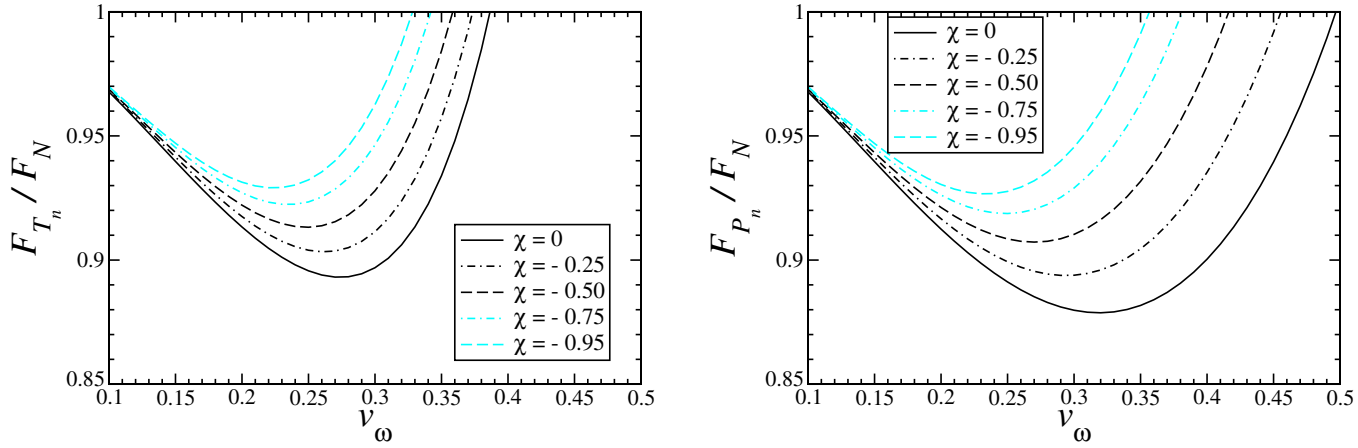

FIG. 6 (color online). Newton-normalized flux in the equal-mass case with both BH spins antialigned (and maximal $\chi = \chi_1 = \chi_2$) with orbital angular momentum when T approximants (left panel) and (lower-diagonal) P approximants (right panel) are used.

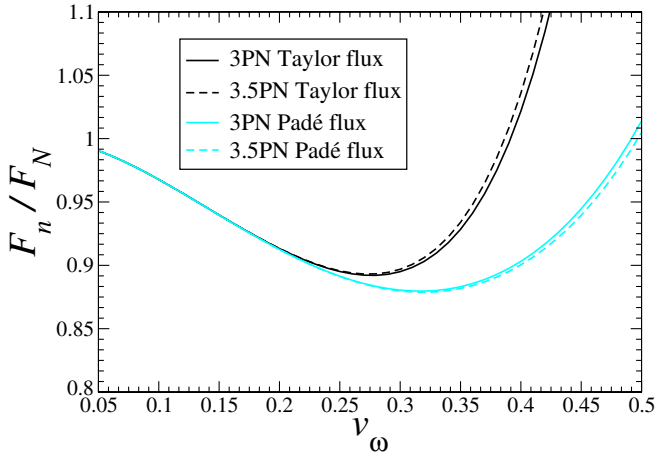

FIG. 7 (color online). Comparison between the T- and (lower-diagonal) P-approximant Newton-normalized flux in the equal-mass, nonspinning case at 3PN and 3.5PN order.

and several values of the dimensionless spin parameter $\chi = \chi_1 = \chi_2$. We notice that the T and P approximants are much closer in the antialigned cases than in the aligned one. Since the calculation of the nonspinning flux function at 3.5PN order has been completed only recently [46], in Fig. 7 we contrast the T and (lower-diagonal) P approximants at 3PN and 3.5PN order for an equal-mass nonspinning binary.

IV. DEFINITIONS OF THE INITIAL AND ENDING CONDITIONS OF TWO-BODY MODELS

As is clear from Figs. 1 and 2, Taylor-expanded Hamiltonians behave badly near the LSSO. Therefore, we propose to use an EOB-resummed Hamiltonian as our best bet for describing, in a physically reliable manner, the nonadiabatic evolution of BH binaries and their transition between inspiral and plunge. For more generality, we shall consider in this section several types of two-body models.

To define a specific model we must make various choices: (i) the choice of a PN-expanded (or "Taylor-expanded") Hamiltonian (say, "TH") versus an EOB-resummed Hamiltonian (say, "EH"); (ii) the choice of a Taylor-expanded flux function (say, "TF") versus a Padé-resummed one (say, "PF"), and finally (iii) the choice of the PN accuracies used both in the Hamiltonian (say, n PN) and the flux function (say, m PN). This leads to models denoted, for instance, THTF(n, m), EHTF(n, m), EHPF(n, m). In addition, as we are here mainly considering the evolution of *spinning* binaries, we shall add an initial letter S to recall that fact. This leads to models denoted as STHTF(n, m), ..., SEHPF(n, m). To simplify, we shall only consider the PN accuracies (2, 2.5) or (3, 3.5). (Note, as discussed above, that because of the appearance of spurious poles in a few tests, we applied in those cases the Padé resummation only to the nonspinning part of the flux.)

An important parameter in our present model building is to decide when to stop the evolution. This issue was already tackled in Ref. [7]. There, because we were using an EOB Hamiltonian, and were considering nonspinning BH's, we found that we could follow the "plunge" (after LSO crossing) down to a (Schwarzschild-like) radius $\simeq 3M$, at which point we could match to a ring-down signal made of least-damped quasinormal modes. It was found in [7] that, contrary to what the usually employed word plunge suggests, the inspiral motion after crossing the LSO was staying "quasicircular," with a kinetic energy in the radial motion staying small in absolute value, and smaller than 0.3 times the kinetic energy in the azimuthal motion down to $R \simeq 3M$. In our spinning evolutions the situation is more complicated (notably when considering large aligned spins, and also, for evident reasons, when considering Taylor-expanded Hamiltonians). We leave to future work a detailed discussion of the matching to ring-down. We decided to stop the evolution as soon as one of the following inequalities ceased to be fulfilled:

$$|\dot{R}| < 0.3|\mathbf{V}_t|, \tag{4.1a}$$

$$P_R^2/B(R) < 0.3P_\phi^2/R^2, \tag{4.1b}$$

$$|\dot{E}_{\rm RR}| > 0.1|\dot{E}_{\rm RR}^{\rm Newt}|, \tag{4.1c}$$

$$R > \alpha M, \tag{4.1d}$$

where $B(R) = D(R)/A(R)$ [see Eqs. (2.11) and (2.12)]. Criteria (4.1a) and (4.1b) ensure that the evolution does not extend too much beyond circularity, on which our formulation for the radiation-reaction force relies. The quantity $\mathbf{V}_t$ is the tangential velocity (i.e., orthogonal to the relative separation vector $\mathbf{X}$). Criterion (4.1c) is used to avoid going into regimes where the GW energy flux goes to zero (e.g., for Taylor-expanded flux at 2.5PN order). Criterion (4.1d) (in which $\alpha \sim 1$ when using the ADM-coordinate Taylor-expanded Hamiltonian, and $\alpha \sim 2$ when using the Schwarzschild-like EOB Hamiltonian) terminates the evolution at a very small radius, in case all of the above criteria fail to take effect.

In all cases, the instantaneous GW frequency at the time when the integration is stopped defines the *ending frequency* for these waveforms. We shall also consider below extended waveforms obtained by matching a ring-down signal when this ending frequency is reached.

A. Initial conditions: quasispherical orbits

(In this section we shall use natural units $c = 1 = G$ and set $M = 1$.)

In the absence of RR, spherical orbits with constant radius and orbital frequency exist under spin-orbit interactions, but cease to exist when spin-spin interactions are present (except in special situations when the spins and the orbital angular momentum are all aligned/antialigned). When radiation reaction is treated adiabatically, an initial spherical orbit will evolve into a sequence of spherical orbits, due to Eq. (3.13). In this section, we formulate a prescription to construct initial conditions for nonadiabatic evolutions, which lead to quasispherical orbits under spin-orbit interaction.

With spin terms kept only up to the spin-orbit order, the Hamiltonian can be rewritten into a simpler form,

$$H(R, P_R, L, \chi_L) = H_{\rm no\ spin}(R, P_R, L) + 2\frac{L\chi_L}{R^3}. \tag{4.2}$$

Here $H_{\rm no\ spin}$ are terms in the Hamiltonian that do not involve spins, and

$$L \equiv |\mathbf{L}|, \qquad \chi_L \equiv \mathbf{S}_{\rm eff} \cdot \hat{\mathbf{L}}. \tag{4.3}$$

In this form, the Hamiltonian depends on four quantities, $\{R, P_R, L, \chi_L\}$, in which L and χ_L both depend on $\{\theta, \phi, P_\theta, P_\phi\}$, while χ_L also depends on the spins. In the absence of radiation reaction, the conditions for spherical orbits written in terms of partial derivatives (indicated by a subscript i) with respect to the four independent variables $\{R, P_R, L, \chi_L\}$ read

$$[\dot{R}]_0 = 0 \Rightarrow [P_R]_0 = 0, \tag{4.4}$$

$$[\dot{P}_R]_0 = 0 \Rightarrow \left[\left(\frac{\partial H}{\partial R}\right)_c\right]_0 = \left[\left(\frac{\partial H}{\partial R}\right)_i\right]_0 = 0. \tag{4.5}$$

(Here the subscript c indicates canonical partial derivatives. In the rest of this section, we shall continue to use i and c to distinguish between these two types of partial derivatives.) With L and χ_L being conserved quantities, conditions (4.4) and (4.5) will remain satisfied if they are initially satisfied—which proves the existence of spherical orbits.

We now construct initial conditions for spherical orbits, *in the absence of radiation reaction*, based on Eqs. (4.4) and (4.5). In numerical evolutions, given a source coordinate frame, $\{\mathbf{e}_x, \mathbf{e}_y, \mathbf{e}_z\}$, we specify spherical orbits with the following initial *kinetic parameters*: the orbital frequency ω_0, the orbital orientation (i.e., the normal direction to the orbital plane $[\hat{\mathbf{L}}_{\rm N}]_0 = (\boldsymbol{X}\times\dot{\boldsymbol{X}})/|\boldsymbol{X}\times\dot{\boldsymbol{X}}|$), the spins $[\mathbf{S}_{1,2}]_0$, and the direction of initial orbital separation $\mathbf{N} = \boldsymbol{X}/|\boldsymbol{X}|$, which can in turn be given by an initial orbital phase $\phi_{\rm orb}$, calculated with respect to the reference direction of $[\mathbf{S}\times\hat{\mathbf{L}}_{\rm N}]_0$,

$$\mathbf{N}_0 = \frac{[\mathbf{S}\times\hat{\mathbf{L}}_{\rm N}]_0}{|[\mathbf{S}\times\hat{\mathbf{L}}_{\rm N}]_0|}\cos\phi_{\rm orb} + \frac{[\hat{\mathbf{L}}_{\rm N}]_0\times[\mathbf{S}\times\hat{\mathbf{L}}_{\rm N}]_0}{|[\mathbf{S}\times\hat{\mathbf{L}}_{\rm N}]_0|}\sin\phi_{\rm orb}. \tag{4.6}$$

We calculate initial values for $\{\mathbf{X}, \mathbf{P}\}$ in three steps:

(1) We first apply a rotation $\mathcal{R}$ such that $[\hat{\mathbf{L}}_{\rm N}]_0 \to \mathbf{e}_z$ and $\mathbf{N}_0 \to \mathbf{e}_x$.

(2) In spherical-polar coordinates, the above step implies

$$\phi_0 = 0, \qquad \theta_0 = \pi/2. \tag{4.7}$$

(The ϕ_0 here should not be confused with the orbital phase $\phi_{\rm orb}$ above.) Then, we specify the initial frequency ω_0 and impose

$$\omega_0 = \dot{\phi}_0 = \left[\left(\frac{\partial H}{\partial P_\phi}\right)_c\right]_0, \qquad 0 = \dot{\theta}_0 = \left[\left(\frac{\partial H}{\partial P_\theta}\right)_c\right]_0, \tag{4.8}$$

$$[P_R]_0 = 0, \qquad \left[\left(\frac{\partial H}{\partial R}\right)_c\right]_0 = 0, \tag{4.9}$$

and solve for the four variables $\{R, P_R, P_\theta, P_\phi\}_0$.

(3) Finally, we apply the inverse rotation $\mathcal{R}^{-1}$ to the entire system, obtaining a set of initial spherical-orbit conditions consistent with the specified initial kinetic parameters.

When radiation reaction is included, we proceed as in Ref. [7] and modify Eq. (4.4) to include a nonzero $\dot{R}$, according to the prediction from adiabatic evolution,

$$[\dot{R}]_0 = \left[\frac{\dot{E}_{\rm RR}}{(dE/dR)_{\rm sph}}\right]_0, \tag{4.10}$$

in order to prevent radial oscillations. [The subscript sph in Eq. (4.10) and below denotes quantities evaluated along spherical orbits.] Equations (4.5) can be kept unchanged, since $\dot{P}_R$ is second order in radiation reaction. We now calculate $(dE/dR)_{\rm sph}$ in terms of the simplified set of independent variables, $\{R, P_R, L, \chi_L\}$. Considering neighboring spherical orbits in an adiabatic sequence, we have

$$dH = \left(\frac{\partial H}{\partial R}\right)_i dR + \left(\frac{\partial H}{\partial P_R}\right)_i dP_R + \left(\frac{\partial H}{\partial L}\right)_i dL + \left(\frac{\partial H}{\partial \chi_L}\right)_i d\chi_L, \tag{4.11}$$

$$\left(\frac{\partial H}{\partial R}\right)_i = 0, \qquad d\left(\frac{\partial H}{\partial R}\right)_i = 0, \qquad P_R = 0, \qquad dP_R = 0. \tag{4.12}$$

It is straightforward to deduce that[3]

$$\left(\frac{dE}{dR}\right)_{\rm sph} = -\frac{(\frac{\partial H}{\partial L})_i(\frac{\partial^2 H}{\partial R^2})_i}{(\frac{\partial^2 H}{\partial R\partial L})_i} + \underbrace{\left[\left(\frac{\partial H}{\partial \chi_L}\right)_i - \frac{(\frac{\partial H}{\partial L})_i(\frac{\partial^2 H}{\partial R\partial \chi_L})_i}{(\frac{\partial^2 H}{\partial R\partial L})_i}\right]\left(\frac{d\chi_L}{dR}\right)_{\rm sph}}_{\text{will be ignored}}. \tag{4.13}$$

The second term on the right-hand side can be ignored, as we argue later in this section, because χ_L is still conserved to a high accuracy even in the presence of radiation reaction. In special configurations with $\hat{\mathbf{L}} = \mathbf{e}_z$ (or equivalently $\theta = \pi/2$, $P_\theta = 0$), we can rewrite Eq. (4.13) in terms of canonical variables in spherical-polar coordinates:

$$\left(\frac{dE}{dR}\right)_{\rm sph} = -\left[\frac{(\partial H/\partial P_\phi)_c(\partial^2 H/\partial R^2)_c}{(\partial^2 H/\partial R\partial P_\phi)_c}\right]_{\theta=\pi/2, P_\theta=0}. \tag{4.14}$$

We also note that, when $\hat{\mathbf{L}}$ is known to be $\mathbf{e}_z$, we can calculate $\dot{E}_{\rm RR}$ from Eq. (3.15) right away using only ω_0 and $[\mathbf{S}_{1,2}]_0$.

We can now construct quasispherical initial conditions when radiation reaction is present. As done in Ref. [7], up to leading order in radiation reaction, we only need to augment our no-radiation-reaction initial conditions with a *nonzero* P_R, with initial values for all other canonical variables unchanged. In order to do so, we *insert* three more steps between steps 2 and 3 above:

(a) During step 2, we have obtained a set of spherical-polar-coordinate initial conditions, for a *rotated system* with $\{\mathbf{N}_0, [\hat{\mathbf{L}}_{\rm N}]_0\} = \{\mathbf{e}_x, \mathbf{e}_z\}$. The canonical angular momentum, $[\mathbf{L}]_0$ of this system, though, will not, in general, be along $\mathbf{e}_z$. However, being orthogonal to $\mathbf{N}_0 = \mathbf{e}_x$, it must be within the $\mathbf{e}_y - \mathbf{e}_z$ plane. We now apply a further rotation $\mathcal{R}'$ around

[3]Using $dP_R = 0$, $(\frac{\partial H}{\partial R})_i = 0$ and Eq. (4.11), we have $(\frac{dE}{dR})_{\rm sph} = (\frac{\partial H}{\partial L})_i(\frac{dL}{dR})_{\rm sph} + (\frac{\partial H}{\partial \chi_L})_i(\frac{d\chi_L}{dR})_{\rm sph}$; using $d(\frac{\partial H}{\partial R})_i = 0$ and $dP_R = 0$, we have $(\frac{\partial^2 H}{\partial R^2})_i + (\frac{\partial^2 H}{\partial R\partial L})_i(\frac{dL}{dR})_{\rm sph} + (\frac{\partial^2 H}{\partial R\partial \chi_L})_i(\frac{d\chi_L}{dR})_{\rm sph} = 0$. We then use the latter equation to eliminate the dependence of $(\frac{dE}{dR})_{\rm sph}$ on $(\frac{dL}{dR})_{\rm sph}$.

$\mathbf{N}_0 = \mathbf{e}_x$ to the entire system, such that afterwards we have $\{\mathbf{N}_0, [\hat{\mathbf{L}}]_0\} = \{\mathbf{e}_x, \mathbf{e}_z\}$, i.e., $\theta_0 = \pi/2$ and $[P_\theta]_0 = 0$.

(b) Now that Eq. (4.14) is applicable and $\dot{E}_{\rm RR}$ is readily obtainable, we insert them into Eq. (4.10) and obtain $[\dot{R}]_0$. (Note that in this process we use the set of initial conditions already obtained for a spherical orbit in the absence of radiation reaction, with $P_R = 0$.) From this $[\dot{R}]_0$, we obtain the initial value of $[P_R]_0$ to insert into our existing set of initial conditions:

$$[P_R]_0 = \frac{[\dot{R}]_0}{[\frac{1}{P_R}(\frac{\partial H}{\partial P_R})_c]_{P_R \to 0}}. \tag{4.15}$$

(c) Gathering our new set of $\{R, \theta, \phi, P_R, P_\theta, P_\phi\}_0$, we obtain the Cartesian-coordinate variables, and apply an inverse rotation $(\mathcal{R}')^{-1}$ to the entire system. (Now again we have $\{N_0, [\hat{\mathbf{L}}_{\rm N}]_0\} = \{\mathbf{e}_x, \mathbf{e}_z\}$, and are ready to proceed to step 3.)

A straightforward analysis of the various error terms allows us to conclude that the fractional error caused by assuming $\chi_L \equiv \mathbf{S}_{\rm eff} \cdot \hat{\mathbf{L}}$ to be constant along the adiabatic evolution is of 3PN order.

We note that our steps 1, 2 (a, b, c), and 3 can still be applied to give initial conditions, even if the Hamiltonian contains spin-spin terms, although the orbits that follow will, in general, have oscillatory radius and orbital frequency, due to the nonexistence of quasispherical orbits. In Fig. 8 we show the evolutions of $\dot{r}/(r\omega)$ with (dark curves) and without (light curves) spin-spin terms, for $(10 + 10)M_\odot$ (left panel) and $(15 + 5)M_\odot$ (right panel) binaries. We start evolution at 40 Hz, with $(\theta_{S_1}, \phi_{S_1}\theta_{S_2}, \phi_{S_2}) = (60°, 90°; 60°, 0°)$, and show the evolution up to 200 Hz.

V. COMPARISON OF WAVEFORMS AND EVALUATION OF OVERLAPS

In harmonic coordinates, the gravitational wave emitted by a binary system at the leading quadrupole order, in terms of metric perturbation at a distance D, is

$$h_{ij} = \frac{H_{ij}}{D} \equiv \frac{2\mu}{D}\frac{d^2}{dt^2}(X_i X_j). \tag{5.1}$$

Using the leading-order equation of motion, $\ddot{X}_k = -MX_k/R^3$, we rewrite the normalized perturbation H_{ij} as

$$H_{ij} = 4\mu\left(V_i V_j - M\frac{X_i X_j}{R^3}\right). \tag{5.2}$$

Here X_i and $V_i \equiv \dot{X}_i$ can be obtained straightforwardly by solving the Hamilton equations. Depending on the wave propagation direction and the orientation of the detector, the metric perturbation h_{ij} has to be contracted with an appropriate "detection tensor" to give the actually detected waveform. For this we refer, for instance, to Sec. IIIC of Ref. [16] and Sec. II of Ref. [15] [in particular, see Eq. (15)].

Following Ref. [15], the parameters in precessing binaries can be distinguished in *binary local parameters* $\{m_1, m_2, S_1, S_2, \theta_{S1}, \theta_{S2}, \phi_{S1} - \phi_{S2}\}$, *binary directional parameters* $\{\theta_L, \phi_L, \phi_{S1} + \phi_{S2}\}$ (which determine the orientation of the binary as a whole in space), and *directional parameters* $\{\Theta, \varphi, \theta, \phi, \psi\}$, describing the GW propagation and the detector orientation (see Table I in Ref. [15] and the discussion around it). To these parameters we need to add the initial time and the initial orbital phase.

In the *precessing* convention introduced in Ref. [15], the GW signal can be neatly written in terms of (i) parameters depending on the observer's location and orientation,

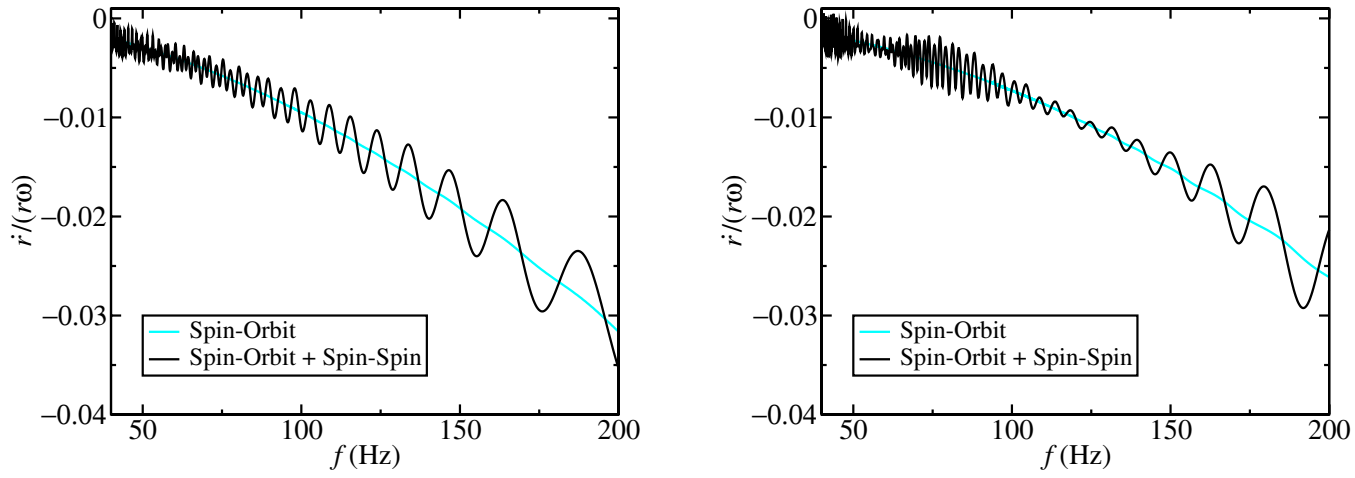

FIG. 8 (color online). Oscillations in $\dot{r}$ when spin-spin interactions are present, in $(10 + 10)M_\odot$ (left panel) and $(15 + 5)M_\odot$ (right panel) binaries. Dark curves show $\dot{r}/(r\omega)$ as functions of $f_{\rm GW}$ when both spin-orbit and spin-spin interactions are take into account, while light curves show the same quantity when only spin-orbit interactions are included.

TABLE I. We list the overlaps between STHTF(3,3.5), used as the target model, and SEHPF(3,3.5), used as the template model, for several binary masses and initial spin orientations. The two black holes are assumed to carry maximal spins $\chi_1 = \chi_2 = 1$, but for comparison we also show the results in the absence of spins. The evolution starts at $f_{\rm in} = 30$ Hz. In the first three columns we list the ending frequency, the LSSO frequency, and the BH radial separation at $t_{\rm fin}$ for the template model, and in the second three columns we show the same quantities but for the target model. The last two columns contain the overlap maximized only over 2 extrinsic parameters $\rho_{\rm max,2}$ and maximized over 5 extrinsic parameters $\rho_{\rm max,5}$, as described in the text. [Notice that for the spin configuration $(60°, 90°, 60°, 0°)$ and masses $(10 + 10)M_\odot$ and $(15 + 5)M_\odot$, due to a pole in the Padé-approximant flux, we apply the Padé resummation only to the nonspinning terms in the flux.]

$(\theta_{S1}, \phi_{S2}, \theta_{S1}, \phi_{S2})$	$f_{\rm fin}^{\rm SEHPF}$ (Hz)	$f_{\rm LSSO}^{\rm SEHPF}$(Hz)	$R_{\rm fin}^{\rm SEHPF}/M$	$f_{\rm fin}^{\rm STHTF}$(Hz)	$f_{\rm LSSO}^{\rm STHTF}$(Hz)	$R_{\rm fin}^{\rm STHTF}/M$	$\rho_{\rm max,2}$	$\rho_{\rm max,5}$
			$(10 + 10)M_\odot$					
No spin	289	285	4.8	287	285	4.2	0.9150	···
(0°, 0°, 0°, 0°)	745	2145	2.5	466	2145	2.8	0.3750	···
(180°, 0°, 0°, 0°)	290	285	4.8	285	285	4.2	0.9166	···
(180°, 0°, 180°, 0°)	145	145	8.1	145	145	7.4	0.5587	···
(60°, 90°, 60°, 0°)	633	873	2.6	502	502	2.6	0.4851	0.5883
(120°, 90°, 60°, 0°)	280	280	4.9	269	269	4.4	0.5420	0.9472
(120°, 90°, 120°, 0°)	187	187	6.7	186	186	6.0	0.6096	0.9536
			$(15 + 15)M_\odot$					
No spin	192	190	4.8	192	190	4.2	0.8137	···
(0°, 0°, 0°, 0°)	497	1430	2.6	311	1430	2.6	0.4550	···
(180°, 0°, 0°, 0°)	193	190	4.8	191	190	4.2	0.8148	···
(180°, 0°, 180°, 0°)	98	97	8.0	97	97	7.4	0.6403	···
(60°, 90°, 60°, 0°)	429	758	2.6	347	347	2.4	0.5067	0.6290
(120°, 90°, 60°, 0°)	185	185	4.9	180	180	4.4	0.5112	0.9456
(120°, 90°, 120°, 0°)	124	124	6.7	124	124	6.7	0.6868	0.9684
			$(15 + 5)M_\odot$					
No spin	267	265	5.2	265	265	4.2	0.6023	···
(0°, 0°, 0°, 0°)	862	1442	2.3	479	1442	2.5	0.3268	···
(180°, 0°, 0°, 0°)	176	175	7.0	177	175	6.2	0.5188	···
(180°, 0°, 180°, 0°)	141	140	8.3	140	140	7.5	0.4445	···
(60°, 90°, 60°, 0°)	715	796	2.4	425	743	2.4	0.4478	0.6111
(120°, 90°, 60°, 0°)	208	207	6.2	208	208	5.3	0.5471	0.7496
(120°, 90°, 120°, 0°)	224	224	5.9	225	225	4.9	0.5735	0.8360

$\{\Theta, \varphi, \theta, \phi, \psi\}$, which are time-independent, initial time and the initial orbital phase (henceforth denoted as extrinsic parameters) and (ii) parameters depending on the details of the dynamics, $\{m_1, m_2, S_1, S_2, \theta_{S1}, \theta_{S2}, \phi_{S1} - \phi_{S2}\}$ (henceforth denoted as intrinsic parameters). The GW signal does not depend on the binary directional parameters, $\{\theta_L, \phi_L, \phi_{S1} + \phi_{S2}\}$, since those parameters can be reabsorbed in the definition of the source frame at initial time and in the directional parameters $\{\Theta, \varphi, \theta, \phi, \psi\}$ through a rigid rotation of the detector-binary system.

The distinction between extrinsic and intrinsic parameters is due originally to Sathyaprakash and Owen [55,56]. Extrinsic parameters are parameters which change the signal shape in such a way that we do not actually need to lay down templates in the bank along those parameter directions, saving computational time. By contrast we need to lay down templates along the directions of the intrinsic parameters. In Refs. [15,16], a semianalytical method to maximize over the extrinsic parameters in precessing binaries has been proposed.

In view of the bad performances of the Taylor-expanded Hamiltonian,[4] we *a priori* expect that the waveforms computed from STHTF models will be significantly different from the SEHPF ones. It remains, however, interesting to *measure their difference* in the data-analysis sense, i.e. to compute the *overlaps* between the two types of waveforms. If it happened that, after maximization over all possible parameters, the overlap between the two types of signals was very close to unity, one could still consider the Taylor models as *effectual* (in the sense of [19]) representations of the EOB models. However, for practical reasons, we did not try to embark on a full maximization of the overlaps. For simplicity, we *only* tackled the maximization over the extrinsic parameters, and *not* on the intrinsic ones. The

[4]We have in mind here the absence of LSSO. Recall also that, when the binary mass ratio is significantly different from 1, one can firmly conclude that the Taylor-expanded Hamiltonian is a poor representation of the dynamics, while the EOB-resummed one is a good one.

TABLE II. Overlaps between STHTF(2,2), used as the target model, and SEHPF(2,2.5), used as the template model, for several binary masses and initial spin orientations. The two black holes are assumed to carry maximal spins $\chi_1 = \chi_2 = 1$, but for comparison we also show the results in the absence of spins. The evolution starts at $f_{\rm in} = 30$ Hz. In the first three columns we list the ending frequency, the LSSO frequency, and the BH radial separation at $t_{\rm fin}$ for the template model, and in the second three columns we show the same quantities but for the target model. The last two columns contain the overlap maximized only over 2 extrinsic parameters $\rho_{\rm max,2}$ and maximized over 5 extrinsic parameters $\rho_{\rm max,5}$, as described in the text.

$(\theta_{S1}, \phi_{S2}, \theta_{S1}, \phi_{S2})$	$f_{\rm fin}^{\rm SEHPF}$ (Hz)	$f_{\rm LSSO}^{\rm SEHPF}$(Hz)	$R_{\rm fin}^{\rm SEHTF}/M$	$f_{\rm fin}^{\rm STHTF}$(Hz)	$f_{\rm LSSO}^{\rm STHTF}$(Hz)	$R_{\rm fin}^{\rm STHTF}/M$	$\rho_{\rm max,2}$	$\rho_{\rm max,5}$
			$(10 + 10)M_\odot$					
No spin	242	237	5.6	237	237	4.5	0.4691	...
(0°, 0°, 0°, 0°)	628	628	2.9	628	628	2.6	0.3170	...
(180°, 0°, 0°, 0°)	237	237	5.6	237	237	4.5	0.4681	...
(180°, 0°, 180°, 0°)	139	139	8.4	139	139	7.6	0.6433	...
(60°, 90°, 60°, 0°)	367	367	4.1	342	342	3.5	0.4197	0.4882
(120°, 90°, 60°, 0°)	234	234	5.7	229	229	4.7	0.4220	0.6015
(120°, 90°, 120°, 0°)	173	173	7.1	172	172	6.3	0.6681	0.9556
			$(15 + 15)M_\odot$					
No spin	158	158	5.6	158	158	4.5	0.4880	...
(0°, 0°, 0°, 0°)	419	419	2.9	419	419	2.6	0.4044	...
(180°, 0°, 0°, 0°)	158	158	5.6	158	158	4.5	0.4885	...
(180°, 0°, 180°, 0°)	93	93	8.4	93	93	7.6	0.7140	...
(60°, 90°, 60°, 0°)	240	238	4.2	241	241	4.1	0.4549	0.5186
(120°, 90°, 60°, 0°)	156	155	5.7	152	152	4.7	0.4827	0.6767
(120°, 90°, 120°, 0°)	115	115	7.1	116	116	6.2	0.7227	0.9442
			$(15 + 5)M_\odot$					
No spin	232	232	5.7	233	232	4.7	0.6111	...
(0°, 0°, 0°, 0°)	608	608	2.9	608	608	2.6	0.2695	...
(180°, 0°, 0°, 0°)	167	166	7.3	166	166	6.5	0.8720	...
(180°, 0°, 180°, 0°)	136	136	8.5	136	136	7.7	0.6743	...
(60°, 90°, 60°, 0°)	352	352	4.2	367	367	3.2	0.2696	0.4978
(120°, 90°, 60°, 0°)	192	192	6.6	191	191	5.7	0.6566	0.8173
(120°, 90°, 120°, 0°)	169	169	7.2	167	167	6.5	0.6207	0.8970

resulting partially maximized overlap is therefore only a lower bound of the fully maximized overlap. Still, this result can be considered as a reasonable measure of the "closeness" between the two sorts of models (especially because we do not wish to use models which would have significantly different physical parameters).

A. Lack of closeness between Taylor and effective-one-body models

In Tables I and II we study the *closeness* (in the sense just defined of overlap maximized only over the extrinsic parameters[5]) between STHTF(3,3.5) and SEHPF(3,3.5), as well as between STHTF(2,2) [6] and SEHPF(2,2.5) models.

We consider three typical binary masses, $(10 + 10)M_\odot$, $(15 + 15)M_\odot$, and $(15 + 5)M_\odot$, and several initial spin orientations.[7] We always fix the pattern functions $F_+ = 1$, $F_\times = 0$ and GW-propagation parameters $\Theta = \pi/4$ and $\varphi = 0$ (for notations and definitions see Sec. IIIC of Ref. [16] and Sec. II of Ref. [15]). The initial frequency is always set to $f_{\rm in} = 30$ Hz and the ending frequency $f_{\rm end}$ is determined by one of the criteria in Eqs. (4.1a)–(4.1d). In Tables I and II, both black holes are assumed to carry maximal spins. We list the ending frequency, the LSSO frequency, and the BH radial separation at $t_{\rm fin}$ for the template and target, together with two types of overlaps: the overlaps maximized over the initial time and initial orbital phase only ($\rho_{\rm max,2}$), and the overlaps maximized over those parameters and $\{\Theta, \varphi, \alpha = f(\theta, \phi, \psi)\}$, as well

[5]More precisely, we do the maximization over the extrinsic parameters of the EOB model. Though this introduces an asymmetry in the definition of the *closeness*, we do not expect this asymmetry to be physically significant.

[6]We use STHTF(2,2) instead of STHTF(2,2.5) because for equal-mass binaries the Taylor-approximant for the flux at 2.5PN order becomes negative for large values of v [19].

[7]For these data we always refer the initial spin directions to the initial direction of the orbital Newtonian angular momentum, as specified in Fig. 4 of Ref. [15], and we set the initial direction of the Newtonian orbital angular momentum along the x axis of the source frame (i.e., we fix $\theta_{\rm L} = \pi/2$ and $\phi_{\rm L} = 0$; see Fig. 3 in Ref. [15]).

($\rho_{\max,5}$), using the semianalytical method suggested in Ref. [16]. Tables I and II also contain the nonspinning case.

As these tables show, the two types of models are not at all ''close to each other.'' The overlaps are indeed quite low, as low as 0.32. The overlaps evidently increase when we maximize over five rather than two extrinsic parameters, but not dramatically, and only for binaries with high and comparable mass, with initial spins lying in the half-space opposite (with respect to the orbital plane) to the initial orbital angular momentum. In this case the dynamical evolution is shorter, since the LSSO occurs at lower frequency (see also Figs. 2 and 3), and the differences in STHTF(3,3.5) and SEHPF(3,3.5) can be compensated by an offset in the extrinsic parameters of the template with respect to the target. Moreover, both the conservative dynamics for circular orbits and the GW flux predicted by SEHPF approximants and STHTF approximants are closer in the antialigned case than in the aligned case, as can be see in Figs. 5 and 6.

However, when the binary mass ratio is significantly different from 1, the number of modulational cycles increases, and the differences in the two models can no longer be compensated by readjusting the template extrinsic parameters. When the initial spins are lying in the same half-space of the orbital angular momentum, the evolution is longer, the LSSO happens at high frequency (see also Figs. 2 and 3), and in this case, even for high, comparable masses, the differences both in the conservative and nonconservative late dynamics in the two models cannot be compensated by a bias in the template extrinsic parameters.

From Table II we notice that all the above considerations apply also at 2PN order, where the differences in the conservative and nonconservative dynamics of STHTF and SEHPF approximants are even larger. We checked that these considerations do not change much when spins are smaller, say half-maximal.

So far, we have confirmed that Taylor models cannot be considered as being effectively close to the EOB ones. Nevertheless, we shall only use EOB models in the following, because they are the only models that could provide us rather robust predictions about the binary close to or beyond the LSSO.

B. Negligible influence of the ''transverse component'' of the radiation-reaction force

Having in mind possible simplifications of the models, we first investigated the relevance of the second term in the R.H.S. of Eq. (3.27), i.e. the component of the radiation-reaction force which is ''transverse,'' in the sense of being directed along L, and therefore orthogonal to the main ''longitudinal term,'' which is parallel to the momentum $\boldsymbol{P}$. In Table III we study the influence of this transverse component of the RR force on the dynamics and the waveforms. For the binary masses $(10 + 10)M_\odot$, $(15 + 5)M_\odot$ and a few initial spin orientations, we evaluate the same quantities of Table I, when including and not including the RR force along L [see the second and third terms in Eq. (3.27)]. We give here only the overlaps maximized over five extrinsic parameters. We find that $\rho_{\max,5}$ is larger than $\sim$0.98 in all cases. We therefore conclude that it would suffice to use a simplified RR force parallel to the linear momentum $\boldsymbol{P}$ (as in the nonspinning circular case). One should, however, include, for better accuracy, in the coefficient of P_i in Eq. (3.27) the spin-dependent terms.

C. Influence of the resummation of the longitudinal part of the radiation reaction

We consider here the longitudinal part of the radiation reaction, i.e. the first term on the R.H.S. of Eq. (3.27). This term is given by the flux function, which was written in Eq. (3.15) above as a straightforward PN expansion. One can therefore either leave this longitudinal component in nonresummed, Taylor form, or choose to resum it by means of Padé approximants. In Table IV we investigate how the choice of the flux function (Taylor expanded or Padé resummed) may affect the dynamics and the waveforms. Using in all cases the EOB Hamiltonian to describe

TABLE III. Effect of radiation-reaction force along L over the binary evolution and waveforms by comparing SEHPF(3,3.5) with no F_L, used as the target model, and SEHPF(3,3.5), used as the template model, for several binary masses and initial spin orientations. The two black holes are assumed to carry maximal spins $\chi_1 = \chi_2 = 1$. The evolution starts at $f_{\rm in} = 30$ Hz. In the first three columns we list the ending frequency, the LSSO frequency, and the BH radial separation at $t_{\rm fin}$ for the template model, and in the second three columns we show the same quantities but for the target model. The last column contains the overlap maximized over 5 extrinsic parameters, $\rho_{\max,5}$, as described in the text. [Notice that for the spin configuration $(60°, 90°, 60°, 0°)$ and masses $(10 + 10)M_\odot$ and $(15 + 5)M_\odot$, due to a pole in the Padé-approximant flux, we apply the Padé resummation only to the nonspinning terms in the flux.]

$(\theta_{S1}, \phi_{S2}, \theta_{S1}, \phi_{S2})$	$f_{\rm fin}^{\rm SEHTF,noF_L}$ (Hz)	$f_{\rm LSSO}^{\rm SEHTF,noF_L}$ (Hz)	$R_{\rm fin}^{\rm SEHTF,noF_L}/M$	$f_{\rm fin}^{\rm SEHTF}$(Hz)	$f_{\rm LSSO}^{\rm SEHTF}$ (Hz)	$R_{\rm fin}^{\rm SEHTF}/M$	$\rho_{\max,5}$
			$(10 + 10)M_\odot$				
$(60°, 90°, 60°, 0°)$	633	872	2.7	660	1211	2.7	0.9860
$(120°, 90°, 120°, 0°)$	187	186	6.7	186	186	6.7	0.9953
			$(15 + 5)M_\odot$				
$(60°, 90°, 60°, 0°)$	743	767	2.3	564	564	2.9	0.9839
$(120°, 90°, 120°, 0°)$	178	177	7.0	179	179	6.9	0.9969

TABLE IV. Effect of Padé and Taylor flux on the binary evolution and waveforms by comparing SEHTF(3,3.5), used as the target model, and SEHPF(3,3.5), used as the template model, for several binary masses and initial spin orientations. The two black holes are assumed to carry maximal spins $\chi_1 = \chi_2 = 1$. The evolution starts at $f_{\rm in} = 30$ Hz. In the first three columns we list the ending frequency, the LSSO frequency, and the BH radial separation at $t_{\rm fin}$ for the template model, and in the second three columns we show the same quantities but for the target model. The last two columns contain the overlap maximized only over 2 extrinsic parameters $\rho_{\rm max,2}$ and maximized over 5 extrinsic parameters $\rho_{\rm max,5}$, as described in the text. [Notice that for the spin configuration $(60°, 90°, 60°, 0°)$ and masses $(10 + 10)M_\odot$ and $(15 + 5)M_\odot$, due to a pole in the Padé-approximant flux, we apply the Padé resummation only to the nonspinning terms in the flux.]

$(\theta_{S1}, \phi_{S2}, \theta_{S1}, \phi_{S2})$	$f_{\rm fin}^{\rm SEHTF}$ (Hz)	$f_{\rm LSSO}^{\rm SEHTF}$(Hz)	$R_{\rm fin}^{\rm SEHTF}/M$	$f_{\rm fin}^{\rm SEHTF}$(Hz)	$f_{\rm LSSO}^{\rm SEHTF}$(Hz)	$R_{\rm fin}^{\rm SEHTF}/M$	$\rho_{\rm max,5}$
			$(10 + 10)M_\odot$				
$(60°, 90°, 60°, 0°)$	632	872	2.6	616	1252	2.6	0.8566
$(120°, 90°, 120°, 0°)$	185	185	6.7	186	185	6.7	0.9762
			$(15 + 5)M_\odot$				
$(60°, 90°, 60°, 0°)$	743	767	2.3	661	772	2.5	0.8232
$(120°, 90°, 120°, 0°)$	178	177	7.0	179	178	6.9	0.9913

the dynamics, we evaluate the overlaps between models using a Taylor flux and models using a Padé flux. (We maximize over the five extrinsic parameters of the EOB model.) We find that, when the initial spins are lying in the same half-space of the orbital angular momentum, after maximization over the five extrinsic parameters, the overlaps are reasonably large (larger than 0.84), but still lower than unity. We obtain much higher overlaps when the initial spins are not lying in the same half-space of the orbital angular momentum. These results are consistent with Figs. 5–7, in the following sense: Figs. 5 and 6 predict that evolutions end at lower frequencies for more antialigned configurations, in which case the Taylor and Padé fluxes are closer to each other for a larger fraction of the evolution, as shown in Fig. 7.

If we assume that the equal-mass flux function is a smooth deformation of the test-mass limit one, since previous findings [7,19,22,53] in the test-mass limit case pointed out the usefulness of Padé-resumming the flux function, we would conclude that Padé-resummed fluxes are better approximants of the numerically determined flux also in the equal-mass case.

D. Negligible influence of the quadrupole-monopole terms

Still in the spirit of trying to simplify the models to their crucial elements, Table V investigates how waveforms are affected by the quadrupole-monopole terms [Eq. (2.20)], and Table VI studies how the evolution obtained by averaging the spin terms over a period may differ from the nonadiabatic evolution. Considering the high values of $\rho_{\rm max,5}$ obtained in both cases, we can say that the quadrupole-monopole interaction and the adiabaticity of the spin terms have little physical effects over the dynamics and waveforms. The differences can be compensated by readjusting the template extrinsic parameters.

E. Influence of the initial orbital phase

Finally, we investigated the influence of the initial orbital phase (all other quantities being fixed) on the nonadiabatic evolution. In an adiabatic evolution in which spin terms are averaged over a period, the joint evolution of $\hat{\mathbf{L}}_{\rm N}$ and $\mathbf{S}$ is not affected by the initial orbital phase. As a consequence, two configurations with the same initial val-

TABLE V. Effect of quadrupole-monopole (QM) interaction on the binary evolution and waveforms by comparing SEHPF(3,3.5) with QM interaction, used as the target model, and SEHPF(3,3.5) without QM terms, used as the template model, for several binary masses and initial spin orientations. The two black holes are assumed to carry maximal spins $\chi_1 = \chi_2 = 1$. The evolution starts at $f_{\rm in} = 30$ Hz. In the first three columns we list the ending frequency, the LSSO frequency, and the BH radial separation at $t_{\rm fin}$ for the template model, and in the second three columns we show the same quantities but for the target model. The last two columns contain the overlap maximized only over 2 extrinsic parameters $\rho_{\rm max,2}$ and maximized over 5 extrinsic parameters $\rho_{\rm max,5}$, as described in the text. [Notice that for the spin configuration $(60°, 90°, 60°, 0°)$ and masses $(10 + 10)M_\odot$ and $(15 + 5)M_\odot$, due to a pole in the Padé-approximant flux, we apply the Padé resummation only to the nonspinning terms in the flux.]

$(\theta_{S1}, \phi_{S2}, \theta_{S1}, \phi_{S2})$	$f_{\rm fin}^{\rm SEHTF,noQM}$ (Hz)	$f_{\rm LSSO}^{\rm SEHTF,noQM}$(Hz)	$R_{\rm fin}^{\rm SEHTF,noQM}/M$	$f_{\rm fin}^{\rm SEHPF}$(Hz)	$f_{\rm LSSO}^{\rm SEHPF}$(Hz)	$R_{\rm fin}^{\rm SEHPF}/M$	$\rho_{\rm max,5}$
			$(10 + 10)M_\odot$				
$(60°, 90°, 60°, 0°)$	650	1257	2.6	633	872	2.6	0.9959
$(120°, 90°, 60°, 0°)$	185	184	6.8	186	186	6.7	0.9988
			$(15 + 5)M_\odot$				
$(60°, 90°, 60°, 0°)$	702	766	2.3	743	767	2.3	0.9823
$(120°, 90°, 120°, 0°)$	178	178	7.0	178	177	7.0	0.9979

TABLE VI. Effect of assuming that spins evolve adiabatically. We compare SEHPF(3,3.5), used as the target model, and SEHPF(3,3.5) obtained by averaging the spin couplings over an orbit, used as the template model, for several binary masses and initial spin orientations. The two black holes are assumed to carry maximal spins $\chi_1 = \chi_2 = 1$. The evolution starts at $f_{\rm in} = 30$ Hz. In the first three columns we list the ending frequency, the LSSO frequency, and the BH radial separation at $t_{\rm fin}$ for the template model, and in the second three columns we show the same quantities but for the target model. The last two columns contain the overlap maximized only over 2 extrinsic parameters $\rho_{\rm max,2}$ and maximized over 5 extrinsic parameters $\rho_{\rm max,5}$, as described in the text. [Notice that for the spin configuration $(60°, 90°, 60°, 0°)$ and masses $(10 + 10)M_\odot$ and $(15 + 5)M_\odot$, due to a pole in the Padé-approximant flux, we apply the Padé resummation only to the nonspinning terms in the flux.]

$(\theta_{S1}, \phi_{S2}, \theta_{S1}, \phi_{S2})$	$f_{\rm fin}^{\rm SEHPF,adiab}$ (Hz)	$f_{\rm LSSO}^{\rm SEHPF,adiab}$(Hz)	$R_{\rm fin}^{\rm SEHPF,adiab}/M$	$f_{\rm fin}^{\rm SEHPF}$(Hz)	$f_{\rm LSSO}^{\rm SEHPF}$(Hz)	$R_{\rm fin}^{\rm SEHPF}/M$	$\rho_{\rm max,5}$
			$(10 + 10)M_\odot$				
$(60°, 90°, 60°, 0°)$	636	1185	2.6	633	872	2.7	0.9666
$(120°, 90°, 120°, 0°)$	186	185	6.7	186	186	6.7	0.9932
			$(15 + 5)M_\odot$				
$(60°, 90°, 60°, 0°)$	699	827	2.3	743	767	2.3	0.9665
$(120°, 90°, 120°, 0°)$	177	177	7.0	178	177	7.0	0.9914

ues for $\hat{\mathbf{L}}_{\rm N}$ and $\mathbf{S}$, but different orbital phases $\phi_{\rm orb}$, will keep the difference between orbital phases (measured with respect to the frame determined by $\hat{\mathbf{L}}_{\rm N}$ and $\mathbf{S}$) unchanged through the evolution. This may not be true in our nonadiabatic evolution for two reasons: (i) the spin-spin interaction Hamiltonian depends explicitly on the separation vector $\mathbf{N}$ [see Eq. (2.17)], and (ii) the evolution depends on the canonical orbital angular momentum, which is not orthogonal to the orbital plane. We study this feature by evolving maximally spinning $(15 + 15)M_\odot$ binaries with initial orbital phases $\phi_{\rm orb}(0)$ (at 40 Hz) equal to 0, $\pi/4$, $\pi/2$, and $3\pi/4$, but all other parameters identical: $(\theta_{S_1}, \phi_{S_1}; \theta_{S_2}, \phi_{S_2}) = (60°, 90°; 60°, 0°)$. In Fig. 9, we compare evolutions of orbital phases of the latter three cases to the first one directly, by plotting

$$\Delta\phi_{\rm orb}(t) \equiv \phi'_{\rm orb}(t) - \phi_{\rm orb}(t), \tag{5.3}$$

with $\phi'_{\rm orb}(t)$ orbital-phase evolutions starting at $\phi'_{\rm orb}(0) = \pi/4$, $\pi/2$, and $3\pi/4$, and $\phi_{\rm orb}(t)$ the orbital-phase evolution starting at $\phi_{\rm orb}(0) = 0$. In this plot, the difference $\Delta\phi_{\rm orb}(t)$ grows in time, and can accumulate up to one cycle by the end of the evolution. However, once we shift

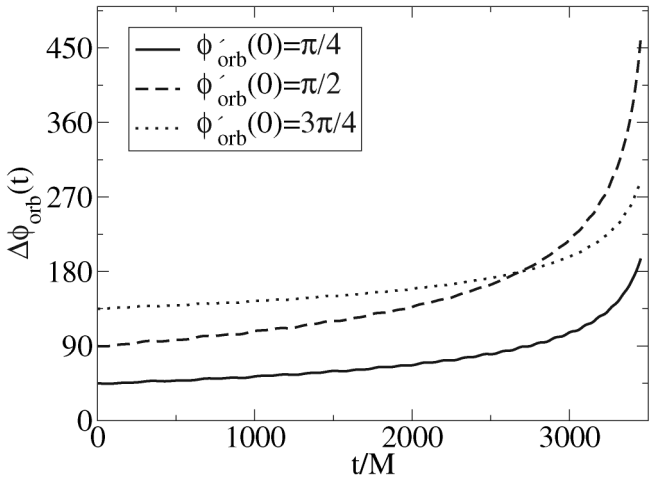

FIG. 9. Direct comparison of orbital phases measured with respect to the frame determined by $\mathbf{S}_{\rm tot} \times \hat{\mathbf{L}}_N$, when different initial orbital phases are used. For maximally spinning $(15 + 15)M_\odot$ binaries, we start evolution at 40 Hz, with $(\theta_{S_1}, \phi_{S_1}; \theta_{S_2}, \phi_{S_2}) = (60°, 90°; 60°, 0°)$, and initial orbital phases of $\phi_{\rm orb}(0) = 0$, and $\phi'_{\rm orb}(0) = \pi/4$, $\pi/2$, and $3\pi/4$. We use the evolution with $\phi_{\rm orb}(0) = 0$ as a reference, and plot (in degrees) the direct differences $\Delta\phi_{\rm orb}(t) \equiv \phi'_{\rm orb}(t) - \phi_{\rm orb}(t)$ in orbital-phase evolution [cf. Eq. (5.3)].

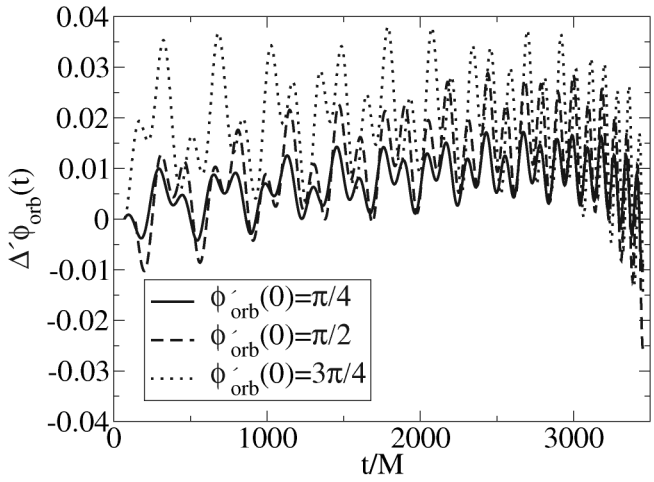

FIG. 10. Comparison of orbital phases measured with respect to the frame determined by $\mathbf{S}_{\rm tot} \times \hat{\mathbf{L}}_N$, when different initial orbital phases are used—with a relative time shift applied to reduce secular growth in the differences. We take the same binary and initial conditions as in Fig. 9, but apply a time shift δt on evolutions with $\phi'_{\rm orb}(0) = \pi/4$, $\pi/2$, and $3\pi/4$, before comparing them to the evolution with $\phi_{\rm orb}(0) = 0$. We plot (in radians) the resulting $\Delta'\phi_{\rm orb}$ [cf. (5.4)], when δt is optimized in the reduction of secular growths in phase differences. The $\delta t/M$ used are 69, 139, and 71, respectively. (The initial orbital period is 338 M.)

the starting time of these evolutions by an appropriate amount (in our cases, smaller than the orbital period), almost all of the secular growth in $\Delta\phi_{\rm orb}(t)$ can be eliminated. In Fig. 10, we plot

$$\Delta'\phi_{\rm orb}(t) \equiv \begin{cases} [\phi'_{\rm orb}(t-\delta t) - \phi_{\rm orb}(t)] - [\phi'_{\rm orb}(0) - \phi_{\rm orb}(\delta t)], & \delta t > 0, \\ [\phi'_{\rm orb}(t-\delta t) - \phi_{\rm orb}(t)] - [\phi'_{\rm orb}(-\delta t) - \phi_{\rm orb}(0)], & \delta t < 0, \end{cases} \tag{5.4}$$

with δt optimized for the elimination of secular growth. (When $\delta t > 0$, $\phi'_{\rm orb}$ is shifted forward in time, and vice versa.) This means, in our nonadiabatic evolutions, the secular evolution of the orbital phase is still *almost* independent from the initial orbital phase. The need for the time shift δt can be traced back to the dependence of the spin-spin interaction Hamiltonian on the separation vector $\mathbf{N}$, and the nonexistence of strictly spherical orbits. Specifically, when we set the initial condition for our nonadiabatic evolution [cf. Sec.], we were imposing that the initial angular velocity at $t = 0$ is half of a particular initial GW angular frequency, $2\pi \times 40$ Hz in cases considered here. However, due to spin-spin coupling, the angular velocity cannot stay constant throughout one cycle, and in most cases the *averaged* angular velocity in the first cycle is slightly *unequal* to the angular velocity we set at $t = 0$—with a difference that depends on the initial orbital phase (i.e., the initial direction of $\mathbf{N}$). Because it is the averaged angular velocity that corresponds to the GW frequency in adiabatic evolutions, nonadiabatic evolutions starting at the *same* nominal initial GW frequency but different initial orbital phases will correspond to adiabatic evolutions with slightly *different* initial frequencies. This will lead to a secular growth in $\Delta\phi_{\rm orb}(t)$; on the other hand, once we impose a small shift δt in the starting time, we can again make the initial frequencies equal, and obtain a $\Delta'\phi_{\rm orb}$ without secular growth.

VI. LOSSES OF ENERGY AND ANGULAR MOMENTUM AND THE WAVEFORM INCLUDING RING-DOWN

In the following, we use as a model the best bet we can make, i.e. the spinning EOB Hamiltonian[8] with a Padé-resummed flux—both being taken to the highest PN accuracy available, i.e. $n = 3$, $m = 3.5$, in the notation used above.

A. Energy released

In Ref. [57], using the nonspinning EOB Hamiltonian at 2PN order, it was found that the energy emitted during the plunge is $\sim 0.7\%$ of M, with a comparable energy loss $\sim 0.7\%$ of M during the ring-down phase. This gives a total energy released beyond the LSSO in the nonspinning case of $\sim 1.4\%$ of M to be contrasted with 4%–5% of M estimated in Ref. [27], where the authors use a combination of numerical and perturbative approximation methods. Note also that Flanagan and Hughes [58] predicted $\sim 10\% M$ for inspiral and plunge, and $\sim 3\% M$ for the ring-down phase.

Here, to have more confidence in our estimates, we decided to use *three different ways* of evaluating the energy radiated in the spinning case. We used, at once, (i) the change along the evolution (between some initial frequency and some final one) in the numerical value of the Hamiltonian (2.15) (δE_H), (ii) the time integral of the square of the numerical third derivative of the leading-order quadrupole moment I_{ij} with $i, j = 1, 2, 3$, i.e.

$$\frac{dE_I}{dt} = \frac{1}{5}\sum_{ij} \frac{d^3 I_{ij}}{dt^3}\frac{d^3 I_{ij}}{dt^3} \qquad I_{ij} = \mu\left(X_i X_j - \frac{1}{3}\delta_{ij} X^k X_k\right), \tag{6.1}$$

and (iii) the time integral of the energy flux carried away by our leading-order quadrupole waveform,

$$\frac{dE_h}{dt} = \frac{1}{20}\sum_{ij} \dot{H}^{\rm TF}_{ij}\dot{H}^{\rm TF}_{ij}, \tag{6.2}$$

with $H^{\rm TF}_{ij}$ being the trace-free part of the normalized metric perturbation, H_{ij} [see Eq. (5.2) above].

In Fig. 11 we compare the accumulated energy release from these three prescriptions, for a $(15 + 15) M_\odot$ maximally spinning binary with a generic set of spin orientations when starting evolution at $f_{\rm GW} = 30$ Hz: $(\theta_{S_1}, \phi_{S_1}; \theta_{S_2}, \phi_{S_2}) = (60°, 90°; 60°, 0°)$. In the left panel, we keep radiation-reaction force at the Newtonian order, i.e., using only the first term of Eq. (3.15), while we use 3.5PN Padé flux in the right panel. As we see from the figure, these prescriptions differ more from each other when 3.5PN radiation reaction is used instead of Newtonian—this is consistent with the fact that both δE_I and δE_h involve quadrupole radiation only; furthermore, for lower frequencies the δE_H curve lies below those of δE_I and δE_h, which is consistent with the fact that post-Newtonian GW luminosity is, in general, smaller than the Newtonian prediction. The difference among δE_I and δE_h can be attributed to the difference between PN (in our case EOB at 3PN) and Newtonian dynamics, which seems to be small till around $f_{\rm GW} = 200$ Hz in our case (which corresponds to $v \approx 0.45$).

Because of the rather satisfactory agreement between the various ways of estimating the energy loss, we use the

[8] We did not investigate the closeness between the models derived from the spinning Hamiltonian used here, or those deduced from the further resummed, Kerr-like EOB Hamiltonian proposed in [5]. In view of the comparison showed in Fig. 3, we expect that the two models are very close to each other.

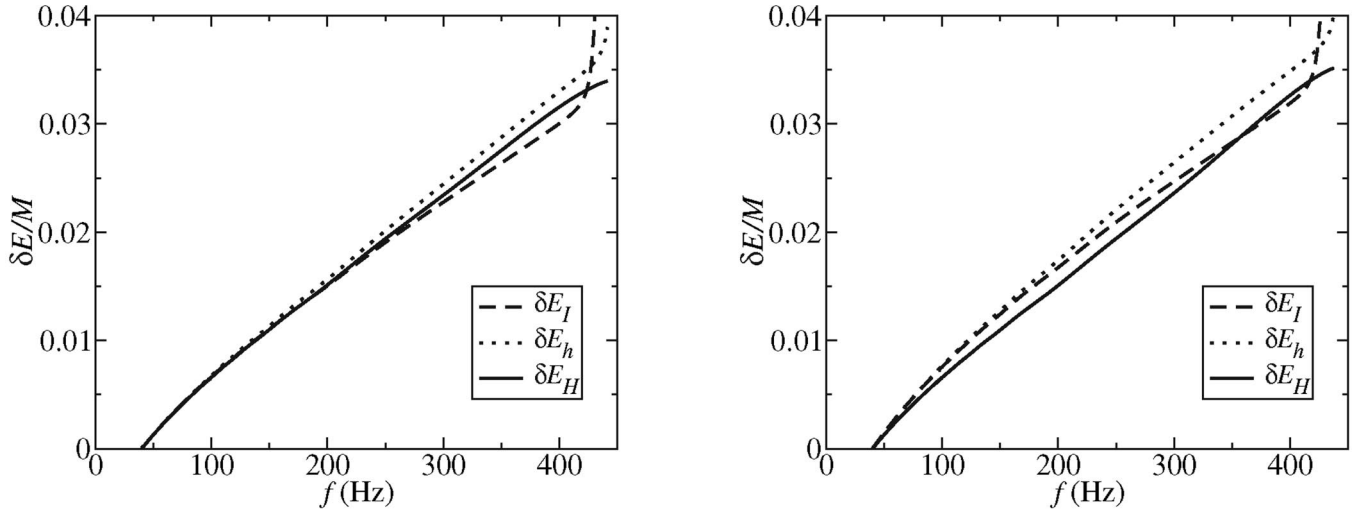

FIG. 11. Comparison between the three different prescriptions, δE_I (dashed curves), δE_h (dotted curves), and δE_H (solid curves), for calculating energy losses. We use Newtonian-order radiation reaction in the left panel, and Padé at 3.5PN order in the right panel. We use the EOB Hamiltonian at 3PN order.

one based on the change in the total EOB Hamiltonian H, because it involves the highest PN accuracy, and hence is the *a priori* best estimate. We will use Padé-resummed fluxes, with combined Hamiltonian and flux PN orders equal to $(n, m) = (3, 3.5)$. In the upper panels of Fig. 12 we plot the accumulative energy loss δE_H starting from $f_{\rm GW} = 40$ Hz as a function of the instantaneous GW frequency f, for $(15 + 15)M_\odot$ (upper left panel) and $(15 + 5)M_\odot$ (upper right panel) binaries, each for 4 sets of initial spin orientations with *maximal spins*: aligned (dark dotted curves), antialigned (light dotted curves), $(\theta_{S_1}, \phi_{S_1}; \theta_{S_2}, \phi_{S_2}) = (60°, 90°; 60°, 0°)$ (denoted by *generic-up*, dark dashed curves), and $(\theta_{S_1}, \phi_{S_1}; \theta_{S_2}, \phi_{S_2}) = (120°, 90°; 120°, 0°)$ (denoted by *generic-down*, light dashed curves), as well as for the nonspinning configuration (dark solid curves). In each panel, we also use vertical grid lines to mark LSSO frequencies. As was shown in [5] and in Fig. 3 above, the 3PN-EOB LSSO for mostly aligned fast-spinning BH's is drastically drawn inwards towards very high orbital frequencies—so high, indeed, that for aligned and generic-up configurations they fall out of the frequency range plotted in Fig. 12. As a consequence, for aligned and generic-up configurations, the dynamical evolutions become rather nonadiabatic even before the formal LSSO is reached.

As we see from the plots, within a given GW frequency interval, binaries tend to emit more energy in configurations where spins are more aligned with the orbital angular momentum. This agrees with the results of [5] and of Figs. 1 and 2 above, showing that more aligned configurations are drawn towards more deeply bound states. This, together with the fact that LSSO frequencies are pushed higher in aligned configurations (as we also see from Figs. 1 and 2), can make the total energy releases in aligned configurations several times more than those in antialigned configurations. In Table VII, we list values of $\delta E_H/M$, accumulated from 40 Hz up to LSSO frequency (if reached) or ending frequency (otherwise) for configurations plotted in Fig. 12. We also list the energy released below 40 Hz. For $(15 + 15)M_\odot$, maximally spinning binaries, the energy released from 40 Hz up to the end of our evolution [determined by one of the criteria (4.1a)–(4.1d)] can range from 0.6% of M (antialigned configuration) to 5% of M (antialigned configuration), with the nonspinning configuration releasing 1.6%–1.8% of M (in which 0.8%–1.1% of M is released before LSSO). For $(15 + 5)M_\odot$ binaries, the range is similar, from 0.5% to 5% of M, with nonspinning configuration releasing 1.2%–1.4% of M (in which 0.7%–0.8% of M is from before the LSSO). We also note that the energies of around 0.8% of M and 0.5% of M are released below 40 Hz, for $(15 + 15)M_\odot$ and $(15 + 5)M_\odot$ binaries, respectively. See also Eq. (4.1) of [5] for an approximate analytical estimate of the energy released down to the LSSO, as a function of both $\eta = m_1 m_2/M^2$ and χ_L.

B. Evolution of the dimensionless rotation parameter J/E^2

An important consistency check of the EOB approach concerns the dimensionless total angular-momentum ratio $|\mathbf{J}|/E^2$ ultimately reached by spinning black hole binaries. Indeed, if the EOB method would, at the end of its validity domain, predict a ratio $|\mathbf{J}|/E^2$ larger than unity, this would preclude to match this end state with the newly born Kerr black hole expected from the coalescence of the two initial (spinning) black holes. This issue was investigated *in the adiabatic* approximation in [5]. There, it was shown that, when using the 3PN-accurate EOB Hamiltonian, the ratio $|\mathbf{J}|/E^2$ estimated *at the LSSO* was *always smaller than unity*. This result was not at all guaranteed in advance,

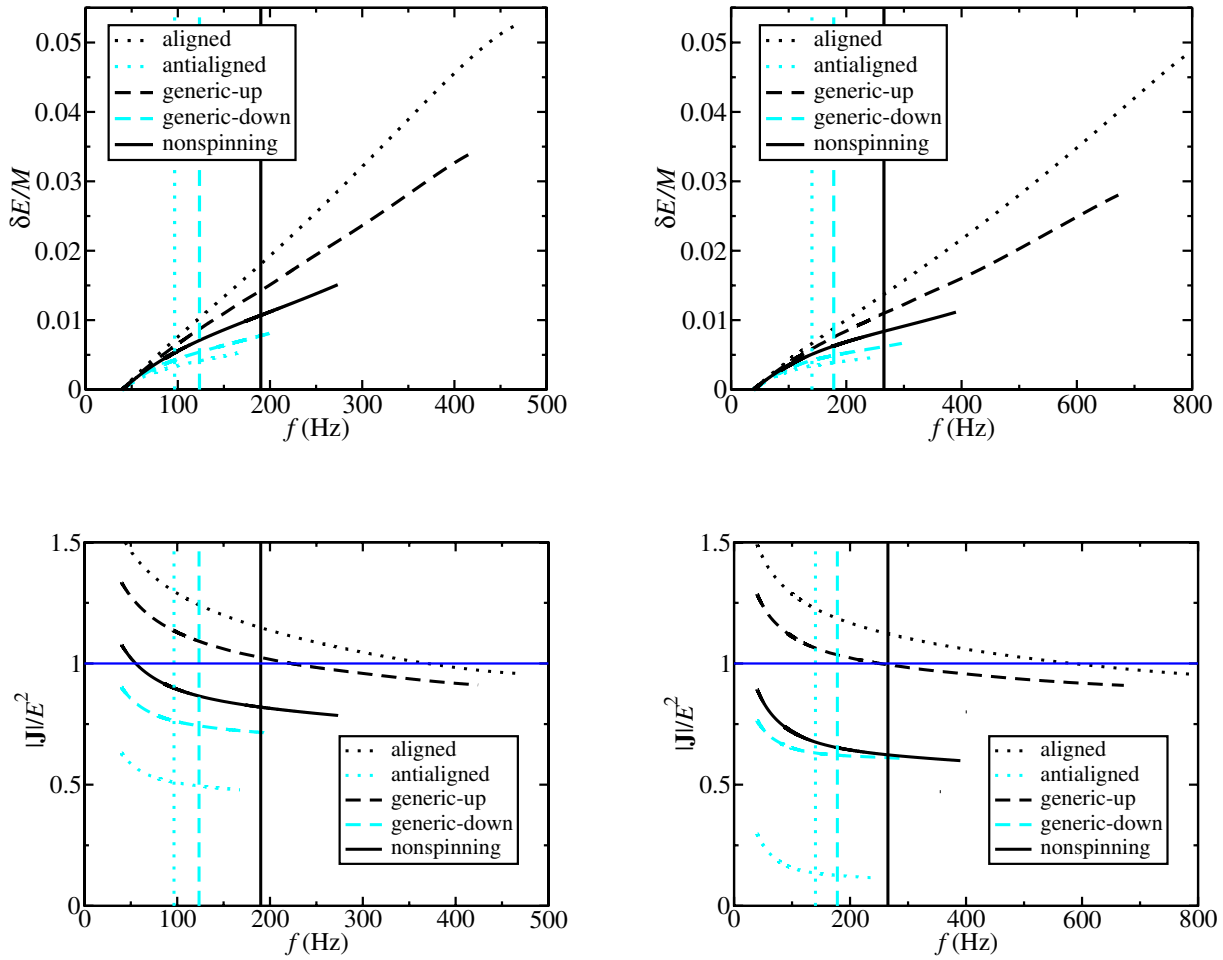

FIG. 12 (color online). Accumulative energy release (upper panels) and instantaneous values of $|\mathbf{J}|/E^2$ (lower panels) of $(15+15)M_\odot$ (left panels) and $(15+5)M_\odot$ (right panels) binaries. LSSO frequencies for the antialigned, generic-down, and nonspinning configurations are shown in vertical grid lines, while LSSOs of generic-up and aligned configurations are above the ranges of our plots. (Spin-spin terms are not included in these evolutions.) We use the SEHPF(3,3.5) model.

TABLE VII. Energy released and the magnitude of angular momentum through the evolution (with spin-spin terms ignored). For nonspinning binaries, and four configurations of maximally spinning binaries, we give the energy released below 40 Hz, from 40 Hz up to the LSSO, and from 40 Hz up to the end of the evolution. (In some cases the evolution stops before LSSO can be reached.) We also show the corresponding values of $|\mathbf{J}|/E^2$. Note that these results do not include the ring-down phase.

$(\theta_{S1}, \phi_{S1}, \theta_{S2}, \phi_{S2})$	$[\delta E_H]_{f<40\mathrm{Hz}}/M$	f_{LSSO} (Hz)	$[\delta E_H]^{40\mathrm{Hz}}_{\mathrm{LSSO}}/M$	$[\lvert\mathbf{J}\rvert/E^2]_{\mathrm{LSSO}}$	f_{fin}	$[\delta E_H]^{40,\mathrm{Hz}}_{\mathrm{fin}}/M$	$[\lvert\mathbf{J}\rvert/E^2]_{\mathrm{fin}}$
			$(15+15)M_\odot$, 3PN				
No spin	0.0082	190	0.0107	0.82	325	0.0182	0.77
(0°, 0°, 0°, 0°)	0.0086	(1430)	⋯	⋯	474	0.0527	0.96
(180°, 0°, 180°, 0°)	0.0077	97	0.0033	0.51	194	0.0064	0.47
(60°, 90°, 60°, 0°)	0.0084	(760)	–	–	440	0.0352	0.91
(120°, 90°, 120°, 0°)	0.0079	123	0.0054	0.74	242	0.0101	0.70
			$(15+5)M_\odot$, 3PN				
No spin	0.0048	265	0.0084	0.62	484	0.0141	0.58
(0°, 0°, 0°, 0°)	0.0049	(1442)	⋯	⋯	819	0.0493	0.95
(180°, 0°, 180°, 0°)	0.0046	140	0.0034	0.14	289	0.0054	0.11
(60°, 90°, 60°, 0°)	0.0049	(793)	⋯	⋯	719	0.0294	0.91
(120°, 90°, 120°, 0°)	0.0047	177	0.0049	0.62	351	0.0080	0.60

and resulted from a delicate competition between the linear increase of $|\mathbf{J}|$ when increasing the (aligned) spin of the individual BH's, and its nonlinear decrease because of the displacement of the LSSO towards smaller radii for aligned spinning configurations. It was found in [5] that the maximum of $(|\mathbf{J}|/E^2)_{\rm LSSO}$ was about 0.83, and was reached for $\chi_L \simeq +0.3$.

The fact that this maximum value is significantly below 1 leaves room for not running into any consistency problem even when taking into account the further changes of both E and $\boldsymbol{J}$ during the plunge that follows the crossing of the LSSO. Though our present attack on the problem does not properly consider the final matching between the plunge and the formation of a final Kerr hole, it goes beyond previous treatments using adiabatic approximation. In the lower panels of Fig. 12, we plot the continuous time evolution of the ratio $|\mathbf{J}|/E^2$ during the late stages of the inspiral and its subsequent nonadiabatic ending (which, in many cases, except in fact for the most dangerous aligned, is a post-LSSO plunge). It is convenient to use the gravitational-wave frequency $f_{\rm GW}$ to label the "time" along this evolution. Satisfactorily, we observe that, for all the binaries we have considered, $|\mathbf{J}|/E^2$ decrease to below 1 before either the LSSO or the end of our evolution, whichever comes first. This means there are no *a priori* obstacles to having a Kerr black hole form right after the end of the nonadiabatic "quasiplunge." This means also that, contrary to an early suggestion [58] based on rather coarse estimates, there is no ground for expecting a large emission of gravitational waves between the plunge and the merger. In Table VII we also list the values of $|\mathbf{J}|/E^2$, at LSSO frequency (if reached) and ending frequency, for SEHPF(3,3.5) models.

In a pioneering work, Baker *et al.* [28] evaluated by a 3D numerical simulation the energy radiated from moderately spinning BH binaries with spins aligned or antialigned with the orbital angular momentum. They started the (very short) numerical evolution close to the LSSO predicted by the effective potential method of Pfeiffer *et al.* [43]. As already mentioned above, the numerical initial data chosen in these works rely only on an initial-value-problem (IVP) formulation, and significantly differ both from the numerical initial data constructed by the HKV method [24,41] and from the predictions made by the EOB method (while the HKV and EOB results are quite close to each other [23,42]). One should probably wait until HKV-type initial data for spinning BH's are evolved until coalescence to meaningfully compare their results with the results derived above for energy releases within the EOB approach. However, to have an idea of the current distance between analytical estimates and numerical ones, we have determined the energy released between the LSSO and the final frequency, at 2PN and 3PN order, for two of the spin configurations investigated by Baker *et al.* For spins aligned (antialigned) and $\chi_1 = \chi_2 = 0.17$ ($\chi_1 = \chi_2 = 0.25$), we find that the energy released is $\sim$(0.6–0.9)%M [$\sim$ (1–3)%M]. Baker *et al.* found $\sim$(1.7–1.9)%M and $\sim$(1.9–2.1)%M, respectively. It should be noted that the energy release evaluated by Baker *et al.* includes also the ring-down phase. Ours does not.

C. Complete waveforms describing the nonadiabatic inspiral and coalescence of precessing binary black holes

Finally, though we have not yet carefully studied at which stage we could meaningfully join our "quasiplunge" evolution to the formation of a ringing BH, we have decided, to show the promise of a purely analytical EOB-base approach, to follow Ref. [7] in matching (by requiring first-order continuity of the emitted waveform) the end of our waveform [here defined by the first violation of the "adiabatic criteria" (4.1a) and (4.1b)] to a ring-down

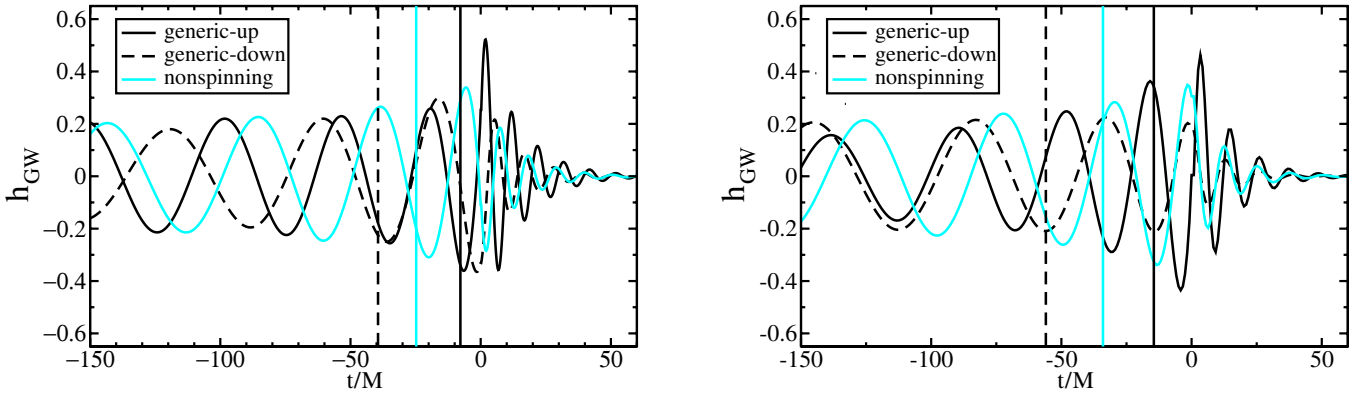

FIG. 13 (color online). Inspiral waveforms (which end at $t = 0$ in our plot) matched to ring-down waveforms for nonspinning (light solid curve) and half-maximally spinning $(15 + 15)M_\odot$ binaries (left panel) and $(15 + 5)M_\odot$ binaries (right panel) in the generic-up (dark solid curve) and generic-down (dark dashed curve) configurations. We start our evolutions at 40 Hz, and use $(F_+, F_\times; \Theta, \varphi) = (1, 0; \pi/4, 0)$. In the plot, we mark the position of the LSSO with solid curves. The waveforms have been shifted in time such that the end of the inspiral occurs at $t/M = 0$.

waveform generated from the lowest $l = m = 2$ quasinormal mode of a Kerr black hole. We determine the mass and spin parameters of the final hole by the energy and angular momentum of the binary at the end of our evolution:

$$M_{\rm BH} = E_{\rm fin}, \qquad a_{\rm BH} = [|\mathbf{J}|/E^2]_{\rm fin}. \tag{6.3}$$

In Fig. 13, we plot the complete waveforms, so obtained, for nonspinning and maximally spinning $(15 + 15)M_\odot$ binaries in the generic-up and generic-down configurations (these refer to the configuration at $f_{\rm GW} = 40$ Hz, the starting point of evolution). We have shifted these waveforms in time so that the end of inspiral evolutions happens at $t = 0$. Notice that at this stage the waveform which includes the ring-down phase should be considered as an example. Indeed, by restricting ourselves to the quasinormal mode $l = m = 2$, we have tacitly assumed that the total angular momentum at the time the ring-down phase starts is dominated by the orbital angular momentum. However, this is not generally the case when spins are present and the quasinormal modes with $l \neq 2$ might be excited as well, and contribute to the waveform. A more thorough analysis is left for the future.

VII. CONCLUSIONS

We provided a first attack on the problem of analytically determining the gravitational waveforms emitted during the last stages of dynamical evolution of precessing binaries of spinning black holes, i.e. during the nonadiabatic ending of the inspiral phase, and its transition to a plunge. We reviewed the various available Hamiltonian descriptions of the dynamics of spinning BH binaries, and studied (following [5]) the characteristics of the stable spherical orbits that exist when spin-spin effects are neglected compared to spin-orbit ones. We derived the contribution to radiation reaction (for quasicircular orbits) which is linear in the spins. Our results agree with the corresponding recent results of [33]. We then used this analytical description of the radiation-reaction-driven inspiral of spinning binaries to construct nonadiabatic models of coalescing binary waveforms. We compared the various models and concluded, in confirmation of previous results, that our current best bet for a nonadiabatic model describing the transition from adiabatic inspiral to plunge is obtained by combining (i) an EOB [6,7], 3PN-accurate [21] resummed Hamiltonian, including spin-dependent interactions [5], with (ii) Padé-resummed radiation-reaction force (including spin terms). Conclusion (i) is rather robust, since, as Fig. 1 shows, the PN-expanded Hamiltonian does not show any LSSO and differs significantly from the PN-expanded, analytically computed function $E(\Omega)$; conclusion (ii) is based on the assumption that the flux function in the equal-mass case is a smooth deformation of the test-mass limit result. Since in the latter case Padé approximants were shown [19,53] to have better agreement with exact numerical flux functions, we would conclude that this is also true in the equal-mass case.

Our main results, obtained by means of this best bet EOB model, are as follows:

(1) An estimate of the energy and angular momentum released by the binary system during its last stages of evolution: inspiral, transition from inspiral to plunge, and plunge;
(2) The finding (which confirms the conclusions of [5]) that the dimensionless rotation parameter J/E^2 is always smaller than unity at the end of the inspiral;
(3) The construction of complete waveforms, approximately describing the entire gravitational-wave emission process from precessing binaries of spinning black holes: adiabatic inspiral, nonadiabatic transition between inspiral and plunge, plunge, merger, and ring-down. Following [7] these waveforms were constructed by matching a quasinormal-mode ring-down to the end of the plunge signal. These tentative complete waveforms are preliminary because we did not include here a careful study of how to join, in a physically motivated manner, the last stages of the plunge to the merger phase. They extend, however, the (better justified) complete waveforms constructed in [7] to the more general case of spinning and precessing binaries.

ACKNOWLEDGMENTS

A. B. thanks the Max-Planck Institut für Gravitationsphysik (Albert-Einstein-Institut) for support during her visit. Y. C.'s research is supported by the Alexander von Humboldt Foundation, and by NSF Grant No. PHY-0099568 (during his stay at Caltech); he also thanks the Institut d'Astrophysique de Paris (CNRS) for support during his visit.

[1] A. Abramovici *et al.*, Science **256**, 325 (1992); http://www.ligo.caltech.edu.
[2] B. Caron *et al.*, Classical Quantum Gravity **14**, 1461 (1997); http://www.virgo.infn.it.
[3] H. Lück *et al.*, Classical Quantum Gravity **14**, 1471 (1997); http://www.geo600.uni-hannover.de.
[4] M. Ando *et al.*, Phys. Rev. Lett. **86**, 3950 (2001); http://tamago.mtk.nao.ac.jp.
[5] T. Damour, Phys. Rev. D **64**, 124013 (2001).
[6] A. Buonanno and T. Damour, Phys. Rev. D **59**, 084006

(1999).
[7] A. Buonanno and T. Damour, Phys. Rev. D **62**, 064015 (2000).
[8] T. A. Apostolatos, C. Cutler, G. J. Sussman, and K. S. Thorne, Phys. Rev. D **49**, 6274 (1994).
[9] L. E. Kidder, Phys. Rev. D **52**, 821 (1995).
[10] T. A. Apostolatos, Phys. Rev. D **52**, 605 (1995).
[11] T. A. Apostolatos, Phys. Rev. D **54**, 2421 (1996).
[12] T. A. Apostolatos, Phys. Rev. D **54**, 2438 (1996).
[13] P. Grandclément, V. Kalogera, and A. Vecchio, Phys. Rev. D **67**, 042003 (2003).
[14] P. Grandclément and V. Kalogera, Phys. Rev. D **67**, 082002 (2003).
[15] A. Buonanno, Y. Chen, and M. Vallisneri, Phys. Rev. D **67**, 104025 (2003).
[16] Y. Pan, A. Buonanno, Y. Chen, and M. Vallisneri, Phys. Rev. D **69**, 104017 (2004).
[17] A. Buonanno, Y. Chen, Y. Pan, and M. Vallisneri, Phys. Rev. D **70**, 104003 (2004).
[18] P. Grandclément, M. Ihm, V. Kalogera, and K. Belczynski, Phys. Rev. D **69**, 102002 (2004).
[19] T. Damour, B. R. Iyer, and B. S. Sathyaprakash, Phys. Rev. D **57**, 885 (1998).
[20] T. Damour, B. R. Iyer, and B. S. Sathyaprakash, Phys. Rev. D **62**, 084036 (2000).
[21] T. Damour, P. Jaranowski, and G. Schäfer, Phys. Rev. D **62**, 084011 (2000).
[22] T. Damour, B. R. Iyer, and B. S. Sathyaprakash, Phys. Rev. D **63**, 044023 (2001); **66**, 027502 (2002).
[23] T. Damour, E. Gourgoulhon, and P. Grandclément, Phys. Rev. D **66**, 024007 (2002).
[24] P. Grandclément, E. Gourgoulhon, and S. Bonazzola, Phys. Rev. D **65**, 044021 (2002).
[25] A. Buonanno, Y. Chen, and M. Vallisneri, Phys. Rev. D **67**, 024016 (2003).
[26] T. Damour, B. R. Iyer, P. Jaranowski, and B. S. Sathyaprakash, Phys. Rev. D **67**, 064028 (2003).
[27] J. Baker, B. Brügmann, M. Campanelli, C. O. Lousto, and R. Takahashi, Phys. Rev. Lett. **87**, 121103 (2001).
[28] J. Baker, M. Campanelli, C. O. Lousto, and R. Takahashi, Phys. Rev. D **69**, 027505 (2004).
[29] V. Kalogera, Astrophys. J. **541**, 319 (2000).
[30] T. Damour and G. Schäfer, Nuovo Cimento Soc. Ital. Fis. B **101**, 127 (1988).
[31] P. Jaranowski and G. Schafer, Phys. Rev. D **57**, 7274 (1998); **63**, 029902(E) (2001).
[32] E. Poisson, Phys. Rev. D **57**, 5287 (1998).
[33] C. M. Will, Phys. Rev. D **71**, 084027 (2005).
[34] T. Damour, P. Jaranowski, and G. Schafer, Phys. Lett. B **513**, 147 (2001).
[35] T. Damour, P. Jaranowski, and G. Schafer, Phys. Rev. D **62**, 021501 (2000); **63**, 029903(E) (2001).
[36] L. E. Kidder, C. M. Will, and A. G. Wiseman, Phys. Rev. D **47**, 3281 (1993).
[37] N. Wex and G. Schafer, Classical Quantum Gravity **10**, 2729 (1993).
[38] B. M. Barker, S. N. Gupta, and R. D. Haracz, Phys. Rev. **149**, 1027 (1966).
[39] B. M. Barker and R. F. O'Connell, Phys. Rev. D **2**, 1428 (1970); Gen. Relativ. Gravit. **11**, 149 (1979); **5**, 539 (1974).
[40] K. S. Thorne and J. B. Hartle, Phys. Rev. D **31**, 1815 (1985).
[41] G. B. Cook, Phys. Rev. D **65**, 084003 (2002).
[42] G. B. Cook and H. P. Pfeiffer, Phys. Rev. D **70**, 104016 (2004).
[43] H. P. Pfeiffer, S. A. Teukolsky, and G. B. Cook, Phys. Rev. D **62**, 104018 (2000).
[44] L. Blanchet, Phys. Rev. D **65**, 124009 (2002).
[45] T. Damour, P. Jaranowski, and G. Schafer, Phys. Rev. D **62**, 044024 (2000).
[46] L. Blanchet, T. Damour, and G. Esposito-Farese, Phys. Rev. D **69**, 124007 (2004).
[47] Y. Itoh, Phys. Rev. D **69**, 064018 (2004).
[48] T. Damour, P. Jaranowski, and G. Schäfer, Phys. Rev. D **63**, 044021 (2001).
[49] V. de Andrade, L. Blanchet, and G. Faye, Classical Quantum Gravity **18**, 753 (2001).
[50] L. Blanchet, B. R. Iyer, and B. Joguet, Phys. Rev. D **65**, 064005 (2002); **71**, 129902(E) (2005).
[51] L. Blanchet, Classical Quantum Gravity **15**, 113 (1998).
[52] L. Blanchet, T. Damour, G. Esposito-Farèse, and B. R. Iyer, Phys. Rev. Lett. **93**, 091101 (2004).
[53] E. K. Porter and B. S. Sathyaprakash, Phys. Rev. D **71**, 024017 (2005).
[54] M. Shibata (private communication).
[55] B. S. Sathyaprakash, Phys. Rev. D **50**, R7111 (1994).
[56] B. J. Owen, Phys. Rev. D **53**, 6749 (1996).
[57] A. Buonanno and T. Damour, IXth Marcel Grossmann Meeting, Rome, 2000 (gr-qc/0011052).
[58] É. É. Flanagan and S. A. Hughes, Phys. Rev. D **57**, 4535 (1998).